Remote Sensing of Environment 295 (2023) 113659

Contents lists available at ScienceDirect

Remote Sensing of Environment

journal homepage: www.elsevier.com/locate/rse

Analytical framework based on thermodynamics to estimate spatially distributed surface energy fluxes from remotely sensed radiations

Mayank Gupta [a], Martin Wild [b], Subimal Ghosh [c,d,*]

[a] Centre for Urban Science and Engineering, Indian Institute of Technology Bombay, Mumbai 400076, India
[b] ETH Zurich, Institute for Atmospheric and Climate Science, 8001 Ziirich, Switzerland
[c] Interdisciplinary Program in Climate Studies, Indian Institute of Technology Bombay, Mumbai 400076, India
[d] Department of Civil Engineering, Indian Institute of Technology Bombay, Mumbai 400076, India

ARTICLE INFO

Edited by Jing M. Chen

Keywords:
Surface eneregy balance
Thermodynamics
Satellite based radiation
Radiation balance

ABSTRACT

The Limited surface observations of turbulent heat fluxes result in incomplete knowledge about the surface energy balance that drives the climate system. The highly parameterized surface energy balance models suffer from significant uncertainties. Remote sensing information of incoming and outgoing radiation fluxes are important input variables for turbulent heat flux models, though analytical solutions of surface energy budget from these variables are yet to be derived. Here, we developed a novel, purely physics-based analytical method grounded on the thermodynamic principle of maximum power. The approach derives the total turbulent heat flux only from the four inputs of incoming and outgoing longwave and shortwave radiations at the land surface, which are available from remotely sensed satellite data. The proposed approach does not use any parameterization, unlike the existing surface energy balance models, and hence does not suffer from uncertainty due to the same. We validated our methodology with 102 eddy covariance observation stations around the globe with different land use land covers from FLUXNET2015 and available urban datasets. Based on monthly averages of the total turbulent flux estimates for the eddy covariance sites, we observed root-mean-square error (RMSE) of 23.2 ± 10.9 Wm^{-2}, a mean bias error (MBE) of 11.9 ± 13.1 Wm^{-2} and R^2 value of 0.86 ± 0.15. Using the satellite observations of radiation fluxes from CERES at a spatial resolution of 1^0, we obtained the global flux field of total turbulent flux (Q_J) and land surface heat storage (ΔQ_s) fluxes. On validation of Q_J with FLUXNET sites for six grids for different land use land cover, we found RMSE of 20.1 ± 7 Wm^{-2}, MBE of 14.4 ± 9 Wm^{-2} and R^2 value of 0.96 ± 0.02. Further, from the evaporative stress factor of GLEAM, which is based on microwave remotely sensed vegetation optical depth and root zone soil moisture, we have obtained spatially distributed global estimates of Sensible(H) and latent heat (LE). In addition, our analytical estimates address the distribution of residual energy associated with the surface energy balance closure problem driven by the land use land cover. The theoretical estimates of all surface energy balance components from remote sensing based observations will improve our understanding of surface warming for different land use land covers across the globe.

List of Symbols

Symbols	Variable Name (Units)
$K_{\downarrow}$	Incoming shortwave radiation flux (Wm^{-2})
$K_{\uparrow}$	Reflected shortwave radiation flux (Wm^{-2})
$L_{\downarrow}$	Incoming longwave radiation flux (Wm^{-2})
$L_{\uparrow}$	Outgoing longwave radiation flux (Wm^{-2})
R_s	Net absorbed shortwave solar radiation flux by the surface (Wm^{-2})
$R_{s,avg}$	Average Surface absorption flux of solar radiation in a day (Wm^{-2})
R_{lnet}	Net outgoing longwave radiation flux (Wm^{-2})
$R_{l,out}$	Flux of terrestrial radiation out of the system (Wm^{-2})
$R_{l,0}$	A constant in longwave linear approximation (Wm^{-2})
Q^*	Net all-wave radiation (Wm^{-2})
Q_J	Total turbulent heat flux (Wm^{-2})
ΔQ_s	Land surface heat storage flux (Wm^{-2})
Q_{RES}	Residual energy flux in Surface energy balance (Wm^{-2})
Q_{Diff}	Differential energy flux (Wm^{-2})

* Corresponding author at: Interdisciplinary Program in Climate Studies, Indian Institute of Technology Bombay, Mumbai 400076, India.
E-mail address: subimal@iitb.ac.in (S. Ghosh).

https://doi.org/10.1016/j.rse.2023.113659
Received 14 November 2022; Received in revised form 12 May 2023; Accepted 29 May 2023
Available online 9 June 2023

H	Sensible Heat flux (Wm^{-2})
LE	Latent Heat flux (Wm^{-2})
H_{opt}	thermodynamic optimal value of Sensible heat flux (Wm^{-2})
LE_{opt}	thermodynamic optimal value of Latent heat flux (Wm^{-2})
T_s	Surface temperature (K)
T_r	Atmospheric radiative temperature (K)
T_{dry}	Effective dry sink temperature (K)
T_a	Effective temperature of atmospheric heat engine (K)
ΔS	Change in Entropy associated with processes (Wm^{-2} $K^{-1)}$
ΔS_{dif}	Entropy of sensible heat diffusion term (Wm^{-2} K^{-1})
ΔS_{pc}	Entropy due to phase change (Wm^{-2} K^{-1})
ΔS_{dv}	Entropy due to water vapour diffusion (Wm^{-2} K^{-1})
G	Convective Power (Wm^{-2})
G_d	Convective Power of dry convective engine (Wm^{-2})
η_{carnot}	Carnot efficiency
D	Frictional Dissipation of mechanical energy (Wm^{-2})
D_K	Dissipation occurs as turbulent dissipation (Wm^{-2})
D_P	Precipitation-induced dissipation (Wm^{-2})
ΔU	Change in Internal Energy of the system (Wm^{-2})
ΔQ_a	Change in atmospheric Heat Storage (Wm^{-2})
f_w	Evaporative Stress fraction
s	Slope of saturation vapour pressure curve
e	partial pressure of water vapour (Pa)
$e_{sat,T}$	Saturation vapour pressure at temperature T (Pa)
γ	Psychometric constant = 65 (Pa K-1)
λ	latent heat of vaporization = 2.5×10^6 ($J\ kg^{-1}\ K^{-1}$)
σ	Boltzmann constant = 5.67×10^{-8} ($Wm^{-2}\ K^{-4}$)

1. Introduction

The energy flow between the surface and the atmosphere largely determines global and regional changes in the climate system due to variations in the atmospheric conditions and surface state(Stephens et al., 2012; Von Schuckmann et al., 2016). The surface energy balance (SEB) is fundamental to assessing this energy exchange (Wild et al., 2013). It disentangles the surface feedback through the competing ecohydrological, biophysical, geophysical processes, and anthropogenic alterations(Duveiller et al., 2018; Forzieri et al., 2018; Huang et al., 2013). The direct global satellite observations of radiative exchange at the top of the atmosphere combined with the global ocean heat content measurements have established global warming by estimating the changes in Earth's energy imbalance (EEI)(Loeb et al., 2021; Schuckmann et al., 2020; Von Schuckmann et al., 2016). However, there is incoherent knowledge concerning the distribution of this radiative energy and its driving factors at the land surface that is mostly shared by the non-radiative surface energy fluxes (Wild, 2020; Wild et al., 2013). Primarily, the surface heating due to the absorbed solar radiation dissipates as the energy transfer to the cooler atmosphere by the net exchange of terrestrial longwave radiation and exchange energy as turbulent heat in the form of Sensible and Latent heat flux. Further, the surface retains some part of the energy as a land surface heat storage flux.

The different techniques(Liang et al., 2010; Rahman and Zhang, 2019; Yi et al., 2019) to estimate surface fluxes depend highly on site-specific parameters and climatic conditions, creating uncertainty for global assessment(Mueller et al., 2013; Mueller and Seneviratne, 2014; Sheffield et al., 2012). Direct in-situ observations are collected as point measurements from surface stations; for example, FLUXNET(Baldocchi et al., 2001; Chu et al., 2017) is a global network of Eddy covariance (EC) towers but with limited coverage for extrapolating to globally distributed estimates(Chu et al., 2017; Jung et al., 2019). Furthermore, the SEB assessment using the EC towers mostly leaves unexplained residual energy, averaging about 16% of available energy, resulting in a surface energy balance closure problem(Mauder et al., 2020; Stoy et al., 2013). The regional climate models used for the surface energy balance computation require detailed surface characteristics and high-resolution for better performance(Davin et al., 2016; Paul et al., 2018), which makes them computationally intensive(Gutowski et al., 2020). Their outputs in simulating energy exchange are characterized by high uncertainty due to the use of spatially and temporally varying parameters and transfer coefficients, which are not well established(Grimmond et al., 2010). The varied sources of input variables and use of multiple climate models are another sources of uncertainty in SEB simulations (Best et al., 2015; Stephens et al., 2012).

Remote sensing (RS) has been used along with land surface models to improve the spatial estimate of turbulent fluxes. In addition to incoming and outgoing radiations, most of these models used additional RS variables, such as land surface temperature (LST) and vegetation indices (VI), like normalized difference vegetation index (NDVI) and Leaf area index (LAI). Influences of these variables on surface energy fluxes (Bateni and Entekhabi, 2012a) were captured through empirical relationships (Carlson, 2007; Gillies et al., 1997; Kalma et al., 2008; Sandholt et al., 2002). The models SEBAL(Bastiaanssen et al., 1998a, 1998b), SEBS(Su, 2002), Ma et al. (2018), and Song et al. (2016) estimate H by combining RS based instantaneous LST with micrometeorology variables like air temperature, wind speed, and humidity, and calculate LE as SEB residual. LST signature and VI control were further used to improve parameterization related to the boundary layer and canopy conductance and thus the evaporation (therefore LE) (Jiang and Islam, 2001; Mallick et al., 2013, 2014; Sun et al., 2013; Tang et al., 2010; Wang et al., 2006). Other method like land data assimilation system (LDAS) assimilates RS products using techniques such as the Kalman filter(Bateni and Entekhabi, 2012b; Carrera et al., 2015; Xu et al., 2011, 2018) and variational data assimilation(Abdolghafoorian et al., 2017; Bateni et al., 2013; Xu et al., 2019). Most of the approaches, however, are tested regionally, with limited availability of global products. The Global land data assimilation system (GLDAS) provides all fluxes globally by integrating satellite and ground observations with multiple land surface models like Mosaic, Noah, and the Community land model (CLM). Apart from using static data of land cover and vegetation classification from AVHRR and MODIS satellites, GLDAS currently assimilates GRACE terrestrial water storage with meteorological forcing data from NOAA Global Data Assimilation System (GDAS)(Rodell et al., 2004). The Model Tree Ensemble (MTE)(Jung et al., 2011) and the FLUXCOM(Jung et al., 2019) products used EC observations using machine learning (ML) ingested with satellite data such as LST, land cover, and the fraction of absorbed photosynthetically active radiation (fPAR). Further, some satellite data integrated products only provide global evapotranspiration (ET) such as MODIS ET(Mu et al., 2007) and GLEAM (Martens et al., 2017; Miralles et al., 2011), both using Priestley-Taylor eq. (PT)(Priestley and Taylor, 1972) equations. In GLEAM, satellite solar radiation and surface meteorology were used as input in the PT equation to estimate potential evaporation. Further, the GLEAM advances by assessing and adding the water stress conditions using microwave retrievals of land surface temperature, soil moisture, and vegetation optical depth, which previous models did not effectively consider. Although RS-based and assimilated models greatly aid in studying global land-surface interactions and water budgets, the uncertainties are associated with global meteorological forcing data, empirical settings with parameters and predictor variables, the broad classification of heterogenous signals such as land cover, use of different machine learning algorithms, and the energy balance closure problem.

Direct and generalized physics-based estimates of the turbulent fluxes, from satellite observations, independent of surface inputs and parameterization, address the abovementioned limitations. However, such models are yet to be developed to assess the spatio-temporal land energy feedback to the atmosphere.

Another crucial component of SEB is the land surface heat storage flux. In most of the modeling techniques, it is used as input to estimate turbulent fluxes(Purdy et al., 2016). More importantly, it determines the inertial heat capacity of the land, develops diurnal variation in local

climate, and governs available energy partitioning into sensible and latent heat flux(Meier et al., 2019). Along with the soil layer, it comprises canopy heat storage that constitutes heat storage in land cover, biomass, water content, and photosynthesis in the canopy(Heidkamp et al., 2018; Moore and Fisch, 1986; Oke et al., 1981). Thus, it shows the potential to explain the role of the variation in land characteristics in climate change. These characteristics are mostly neglected in climate models as they are not easy to measure, need to be parameterized, and are assumed to have insignificant value(Stoy et al., 2013). However, the net canopy storage can aggregate up to 15% of net radiation for crop sites(Moore and Fisch, 1986) and 2–6 times more for urban canopies (Roberts et al., 2006; Oke and Cleugh, 1987).

We developed an approach based on principles of thermodynamics to estimate surface fluxes that describe the land-atmosphere as a radiative-convective system. The energy and entropy budget, through the first and second law of thermodynamics, respectively, describes directions, constraints, and limits of energy conversion in this system. We reviewed the studies(Kleidon, 2016; Kleidon et al., 2014; Kleidon and Renner, 2013a, 2018; Pauluis and Held, 2002a,b; Rennó and Ingersoll, 1996) based on thermodynamics describing the energy and water exchange through a natural radiative-convective system in equilibrium or steady state. Here, we updated the existing thermodynamic theory and developed a theoretical method to estimate the turbulent fluxes in the SEB directly for the first time. Unlike previous studies, the method does not need in-situ measured surface heat storage or its complex parameterization, thus bringing an enlightened perspective on the SEB and its closure for different land covers. We derived an analytical expression (details in Theory and Methods) to estimate the turbulent heat fluxes that does not require high computation requirements and eliminates the highly uncertain parameterization inputs like roughness length. The estimated turbulent fluxes are tested with Eddy covariance observations of the FLUXNET2015(Pastorello et al., 2020) database across different ecosystems and land uses classified by the International Geosphere–Biosphere Programme (IGBP). Further, we showed the potential of the proposed approach in estimating the spatially distributed turbulent (Sensible and latent heat) flux fields by taking inputs from the CERES satellite data and global evaporative stress factor. We validated our approach for several grids where in-situ FLUXNET2015 EC observations are available.

The organization of the paper is as follows: Section 2 presents the theory, equations, and a diagrammatic flow of estimation, assisted by Appendix A, for conceptual understanding of thermodynamic principles in deriving the equations. Section 3 explains the data and the processing steps for local and global validation and implementation. Section 4 presents the results with associated discussions, including validation of local and global thermodynamic estimates with EC fluxes, spatial comparison with global land flux products, discussion of global land surface heat storage flux, and analysis of global aggregated values with literature. Section 5 explains the general discussion with the significance of the approach in understanding the fluxes and limitations. Lastly, Section 5 reports the conclusion.

2. Theory

The Surface energy balance (SEB) at the surface-atmosphere interface is given as:

$$R_s - R_{lnet} = Q_J + \Delta Q_s \tag{1}$$

Where,R_s is the net absorbed shortwave solar radiation flux by the surface, the difference between the incoming shortwave radiation ($K_\downarrow$) and the reflected shortwave radiation ($K_\uparrow$)($R_s = K_\downarrow - K_\uparrow$). ΔQ_s is the surface heat storage flux. R_{lnet} is the net longwave radiation flux, given by the difference between the outgoing longwave radiation ($L_\uparrow$) and the incoming longwave radiation ($L_\downarrow$)($R_{lnet} = L_\uparrow - L_\downarrow$). Q_J is the turbulent heat flux, the sum of sensible heat flux (H) and latent heat flux (LE), ($Q_J = H + LE$).

Here, we described the land-atmosphere as a radiative-convective system in a steady-state. The system boundary is comprised of two boundary reservoirs (Fig.1), Surface as a hot reservoir with temperature T_s and free atmosphere as a cold reservoir with atmospheric radiative temperature T_r. The temperature difference between the reservoirs drives the energy transfer from the surface to the atmosphere. The convective process in the atmospheric boundary layer manifests as a heat engine that causes turbulent heat exchange by mechanical motion of heated air parcel. The convective process carries H from the warmer land surface to the cooler atmosphere. In moist conditions, evaporation is critical as it consumes a substantial part of surface energy as latent heat to form water vapour. According to the studies(Kleidon, 2016; Kleidon et al., 2014; Kleidon and Renner, 2013a), the convective process near the land surface establishes such that the water vapour is passively

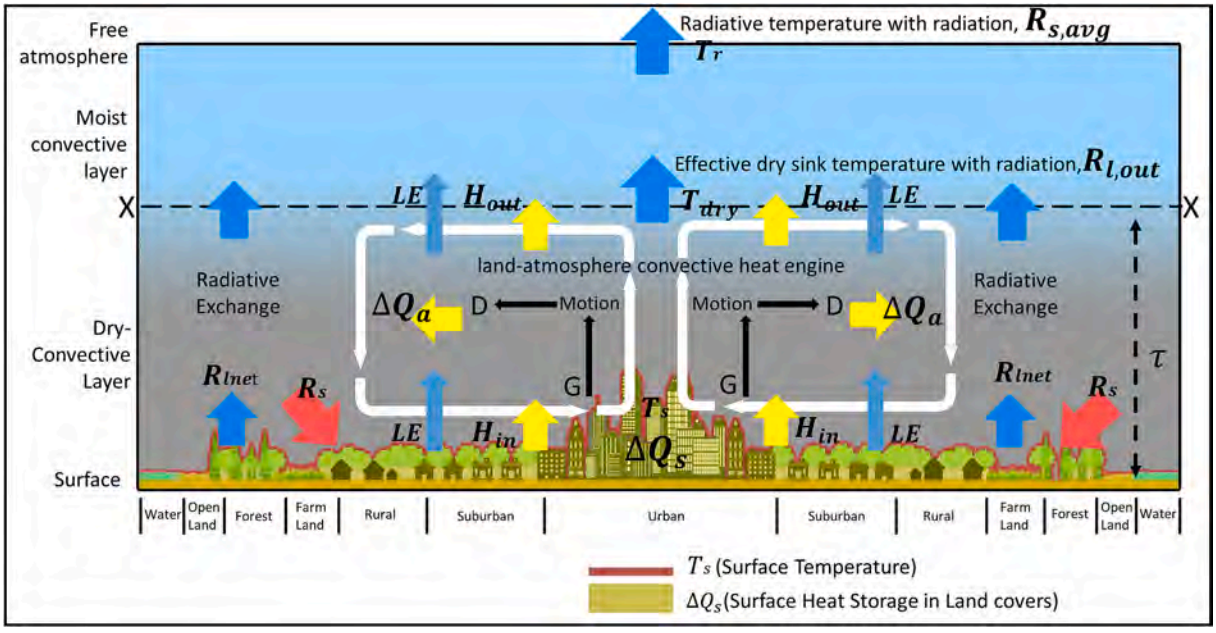

Fig. 1. Schematic diagram of a land-atmospheric convective system using the Thermodynamic theory.

transported as mass exchange with the air parcel in the convective motion until the air parcel saturates and condensation occurs. When the water vapour condenses to form the base of clouds, it releases the latent heat causing the convective motion within the clouds, which ultimately dissipates at the temperature T_r. Hence, two different energy transfer processes exist in two layers (Fig.1). The first is the dry convection near the surface with mechanical updraft and downdraft of air parcels that transport sensible heat and passively transport latent heat as water vapour. The other is the moist convection due to the condensation release of latent heat that develops convective motion in the clouds. Fig.1 shows the schematics of the dry and moist convective layers.

T_r is assessed based on the diurnal behaviour of the land-atmospheric convective system. We used the approach(Kleidon and Renner, 2018) that described the buffering effect of heat in the land-atmospheric system. The surface gets warmer with respect to the cooler atmosphere during the day with the shortwave heating (R_s); however, due to the buffering of this heat into the land surface and the atmosphere, the heat radiates back to the free atmosphere at temperature (T_r) during both day and night, averagely. The average longwave radiation to the free atmosphere from the system during both day and night is $R_{s,avg} = \sigma T_r^4$.

Further, the dynamics of the land-atmospheric energy balance are governed by the first and the second laws of thermodynamics. In a thermodynamic system, the positive irreversible entropy describes the irreversible nature and direction of the physical transformation and limits the energy available for mechanical work in a heat engine. In a dry convective system near the surface, the only irreversibility associated is the molecular diffusion of sensible heat from the surface to the adjacent atmospheric layer and within the atmosphere, creating an irreversible entropy of sensible heat diffusion term (ΔS_{dif}). According to the study (Pauluis and Held, 2002a), the magnitude of ΔS_{dif} is negligible. Hence, the dry convection process works as a perfect heat engine with maximum efficiency, as given by the Carnot limit of maximum power (G_{carnot}) and maximum efficiency (η_{carnot}) (Refer Section A.1 in Appendix A). The irreversibility in moist convection is associated with entropy due to phase change (ΔS_{pc}) and entropy due to water vapour diffusion (ΔS_{dv}). Both entropies are significant and reduce the ability of moist convection to work at maximum efficiency (Pauluis and Held, 2002a,b). Hence, they should be considered in a moist convective process. Therefore, we developed our theory that considered only the dry convective system that occurs near the land surface with negligible entropy following a perfect heat engine.

Another important aspect of irreversibility in the convective process is the frictional dissipation of total kinetic energy generated by mechanical motions of atmospheric flows. In a complete system, the dissipation occurs as turbulent dissipation (D_K) and precipitation-induced dissipation (D_P) that become the parts of the system.D_K is the viscous conversion of mechanical energy of air parcel motion to heat, and D_P is the heat dissipation in microscopic shear zones surrounding hydrometeors. In a dry convective system, we only assume D_K to be associated with sensible heat transport with the dissipation of mechanical energy of air parcel.

The irreversible frictional dissipation of mechanical work associated with the convective motion within the same land-atmospheric system makes the heat engine a Dissipative Heat Engine. The studies(Bister et al., 2011; Pauluis and Held, 2002a) showed that the converted mechanical energy through frictional dissipation increases the internal energy of the system. The heat from frictional dissipation within the engine could not be used as an additional heat source to the engine in addition to the existing heat source to generate mechanical work as it otherwise violates the first law of thermodynamics(Bister et al., 2011). Based on this inference, we derived the power of the dissipative heat engine (G) through energy and entropy budget (Refer to Section A.2, Eq. A7-A10). The heat dissipation of mechanical work (D) and an additional term that depicts the change in the internal energy of the system (ΔU) act such that $G = D = \Delta U$ in a steady state. In dry convection near the land surface, convective heat flux associated with the heat engine is the sensible heat flux ($J_{in} = H$). The internal energy change (ΔU) represents change in the atmospheric heat storage (ΔQ_a) ($\Delta U = \Delta Q_a$) (Fig.1). They are used in the expression for power of dissipative heat engine for dry convection (G_d) (Refer Section A.2, Eq. A11-A12).

Further, considering only the dry convective engine near the surface, we define the effective dry sink temperature (T_{dry}) at which the remaining sensible heat and water vapour is released into the atmosphere. Below the level of T_{dry} (shown by the X-X line in Fig.1), there is no moist convection taking place(Kleidon, 2016). The outgoing radiative flux at T_{dry} is given by $R_{l,out}$. The magnitude of T_{dry} is greater than the T_r.

In dry convection, the sensible heat flux is expressed in terms of convective vertical mass flux of air and the temperature difference between the surface and the effective dry sink temperature following the works(Kleidon, 2016; Kleidon et al., 2014; Kleidon and Renner, 2013a).

$$H = c_p J_m \left(T_s - T_{dry}\right) \tag{2}$$

Where c_p is the specific heat capacity of the air, J_m is the convective mass flux exchange of the air parcel.

As the mass of the air parcel transports water vapour from the surface to the cloud base, it is associated with latent heat expressed as follows:

$$LE = c_p J_m \left(q_s - q_{dry}\right) \tag{3}$$

Where q_s and q_{dry} are the specific humidity of the surface air and the atmosphere. The above equation of LE is associated with the condition that the air had sufficient time and the continuous availability of water to saturate the dry air that rises in the dry convection near the land (Kleidon and Renner, 2013a). In the case of water limiting conditions, the actual LE is given by LE_{lim} based on the water stress factor (f_w) that accounts for water limitation for evaporation such that $LE_{lim} = f_w \times LE$. The corresponding sensible heat flux in that case is given by H_{lim}. As the convection is dependent on the boundary temperatures, the total convective heat flux(Q_J) is same for all conditions such that $Q_J = LE + H = LE_{lim} + H_{lim}$ (Conte et al., 2019).

The difference in specific humidity can be expressed in terms of the temperature difference and the slope of the saturation pressure curve (s) following the study(Kleidon and Renner, 2013a).

$$e_{sat,T} = 611 \times e^{17.6294\frac{T-273.16}{T-35.86}} \tag{4}$$

$$s = \frac{de_{sat,T}}{dt} = \frac{\lambda e_{sat,T}}{R_v T^2} \tag{5}$$

Linear approximation is expressed as:

$$\left(q_s - q_{dry}\right) = \frac{s}{\gamma}\left(T_s - T_{dry}\right) \tag{6}$$

Where λ is the latent heat of vaporization (2.5×10^6 J kg^{-1} K^{-1}) and R_v is the gas constant of water vapour (461 J kg^{-1} K^{-1}).

Therefore,

$$LE = \frac{s}{\gamma} H \tag{7}$$

The value of s is based on the temperature of the air after it comes in contact with the surface to get heated up and saturated with water vapour. In a real scenario, the actual temperature of air never reaches the surface temperature T_s within a finite time scale. Hence,s cannot be computed with T_s. As s varies exponentially with temperature, using T_s for the computation of s will lead to a very high value. Hence, to start with, we estimate the s at the conservative temperature T_r rather than T_s. We compensate for the balance energy later in the convective turbulent energy.

Further, eq. (A8) and (A9) in dry convection becomes:

$$\Delta Q_a = H - H_{out} \tag{8}$$

$$\frac{\Delta Q_a}{T_a} = \frac{H}{T_s} - \frac{H_{out}}{T_{dry}} + \frac{D_k}{T_a} + \Delta S_{dif} \tag{9}$$

Where H_{out} is the release of sensible heat flux out of the dry convective heat engine, D_k is the turbulent frictional dissipation of the mechanical work within the engine itself, and ΔS_{dif} is the entropy due to the diffusion of the sensible heat flux which is negligible.

In the steady-state $G_d = D_k = \Delta Q_a$.We assume the dissipation to be at the surface for near-surface atmospheric convection. Therefore, the power, in this case, is given by:

$$G_d = H\,\frac{T_s - T_{dry}}{T_s} = \Delta Q_a \tag{10}$$

A simple linearization for R_{lnet} is adopted from the study(Conte et al., 2019) (Refer Section A.4, eq. A17-A24) to replace $T_s - T_{dry}$ in eq.10 in terms of heat flux and radiative exchanges (Refer Section A.5, eq. A25-A27) to estimate maximum convective power using expression for G_d:

$$G_d = H.\frac{R_s - R_{l,0} - H\left(1 + \frac{s}{\gamma}\right) - \Delta Q_s}{T_s K_d} \tag{11}$$

Most of the earth system processes are effectively explained by the maximum power limit(Kleidon, 2016; Kleidon et al., 2014; Kleidon and Renner, 2013a). There exists an optimal value of sensible heat flux, H_{opt}, at which the convective power is maximum ($G_{d,max}$). The value of H_{opt} at $G_{d,max}$ is derived by $\frac{dG_d}{dH} = 0$.

Solving $\frac{dG_d}{dH} = 0$, to obtain the analytical expression for H_{opt} which is given as:

$$cH_{opt} = \frac{1}{2}\left(R_s - R_{l,0} - \Delta Q_s\right) \tag{12}$$

Where, $c = 1 + \frac{s}{\gamma}$

The total turbulent flux in terms of surface heat storage based on the maximum convective power is given by the eq. 12.

We use the radiation components, $K_{\downarrow}$,$K_{\uparrow}$,$L_{\uparrow}$, and $L_{\downarrow}$ as input variables to estimate turbulent flux.

The surface net-all wave radiation (Q^*) is given by:

$$Q^* = R_s - R_{lnet} \tag{13}$$

$$Q^* = (K_{\downarrow} - K_{\uparrow}) - (L_{\uparrow} - L_{\downarrow}) \tag{14}$$

According to the surface energy balance:

$$Q^* = Q_J + \Delta Q_s = LE_{opt} + H_{opt} + \Delta Q_s = cH_{opt} + \Delta Q_s \tag{15}$$

Further solving eq. (12) with eqs. (A20), (A22), (13) and (15), we get

$$cH_{opt} = R_{lnet} - R_{l,0} = \quad K_d\left(T_s - T_{dry}\right) \tag{16}$$

To obtain the turbulent flux H_{opt} using eq. (12), we derived the expression $\left(T_s - T_{dry}\right)/T_s$ in terms of cH_{opt} and input variables using equation s (A20), (A22), (A23) and (16) and the expression is given as:

$$\frac{\left(T_s - T_{dry}\right)}{T_s} = \frac{cH_{opt}}{4L_{\uparrow} - 3cH_{opt}} \tag{17}$$

We estimate ΔQ_a in terms of cH_{opt} and input variables from the eqs. (A16), (15), and (A22)

$$\Delta Q_a = 2cH_{opt} - L_{\downarrow} \tag{18}$$

Using eqs. (17), (18) and (10), we get a quadratic equation given as:

$$(1+6c){H_{opt}}^2 - (8L_{\uparrow} + 3L_{\downarrow})H_{opt} + \frac{4\,L_{\downarrow}\,L_{\uparrow}}{c} = 0 \tag{19}$$

Based on the above theory and additional relation given by eq.10, we eliminate the use of surface heat storage to derive the quadratic equation for sensible heat flux (eq. 19).

We solve the eq. (19) using the solution of the quadratic equation to get the two values of H_{opt} with solution as

$$H_{opt1,}\ H_{opt2} = \frac{-B \pm \sqrt{B^2 - 4AC}}{2A} \tag{20}$$

Where:

$A = (1 + 6c)$.

$B = -(8L_{\uparrow} + 3L_{\downarrow})$

$C = \frac{4L_{\downarrow}\,L_{\uparrow}}{c}$

$c = 1 + \frac{s}{\gamma}$

The two solutions of H_{opt}, provides the conditions of maximum and minimum value of turbulent heat flux such that $\frac{dG_d}{dH} = 0$. Further, the profiles may result in the value of H_{opt} greater than Q^* for a few instances, which is impossible for actual conditions. In such cases of, we assume the value of zero in both H_{opt1} and H_{opt2} due to insufficient availability of net energy. We take the maximum value from the resulted two solutions of the H_{opt} to get the best estimate.

$$H_{opt} = max\left\{H_{opt1}, H_{opt2}\right\} \tag{21}$$

We obtain corresponding optimal value of LE_{opt} at maximum convective power from Eq. (7) using the value of H_{opt}. Using Eq. (15) and averaging for monthly to achieve steady-state, we obtain the total turbulent heat flux (Q_J).

Thus, the total turbulent energy is given by the sum of H_{opt} and LE_{opt}. Further, we estimate the T_s based on the above results.

Based on the eqs. 16 and A22, we get:

$$R_{l,out} = L_{\uparrow} - cH_{opt} \tag{22}$$

From eqs. 10, 18, 22 and A24, we get:

$$T_s = \left(\frac{cH_{opt} + 4R_{l,out}}{4R_{l,out}}\right)T_{dry} \tag{23}$$

We found the thermodynamically estimated T_s (Now referred as T_{st}) from eq. 23 is higher than the T_s calculated from $T_s = \left(\frac{L_{\uparrow}}{\sigma}\right)^{\frac{1}{4}}$. The higher value of T_{st} is due to the conservative estimation of the slope of saturation pressure curve (s)(as explained after eq. 7) calculated at the temperature T_r ($T_r < T_s$). The use of T_r in the estimation of s results in a lower value of turbulent flux. We compensate for the differential energy (Q_{Diff}) in outgoing longwave radiation resulting from the differences between T_{st} and T_s. The Q_{Diff} is given as:

$$Q_{Diff} = \sigma {T_{st}}^4 - \sigma {T_s}^4 \tag{24}$$

Thus, the total adjusted turbulent flux is now:

$$Q_J = H_{opt} + LE_{opt} + Q_{Diff} \tag{25}$$

And the land surface heat storage flux (ΔQ_s) using eq. 25 is given by:

$$\Delta Q_s = Q^* - Q_J \tag{26}$$

The diagrammatic flow chart of the equations from the inputs to estimate the surface energy fluxes is shown in Fig. 2.

We then deduce the sensible and latent heat fluxes at the equilibrium partitioning.

$$H_{opt} = \frac{\gamma}{\gamma + s}\,Q_J \tag{27}$$

And

$$LE_{opt} = \frac{s}{\gamma + s}\,Q_J \tag{28}$$

Here, in the eqs. 27 and 28, the s is calculated at T_s following literature(Conte et al., 2019; Kleidon and Renner, 2013b). The eq. 3 describes the condition in which the evapotranspiration is not limited by the water availability. For actual conditions, a stress factor (f_w) is introduced to estimate the actual LE and H. These in the water limiting condition are given by the equations (Conte et al., 2019):

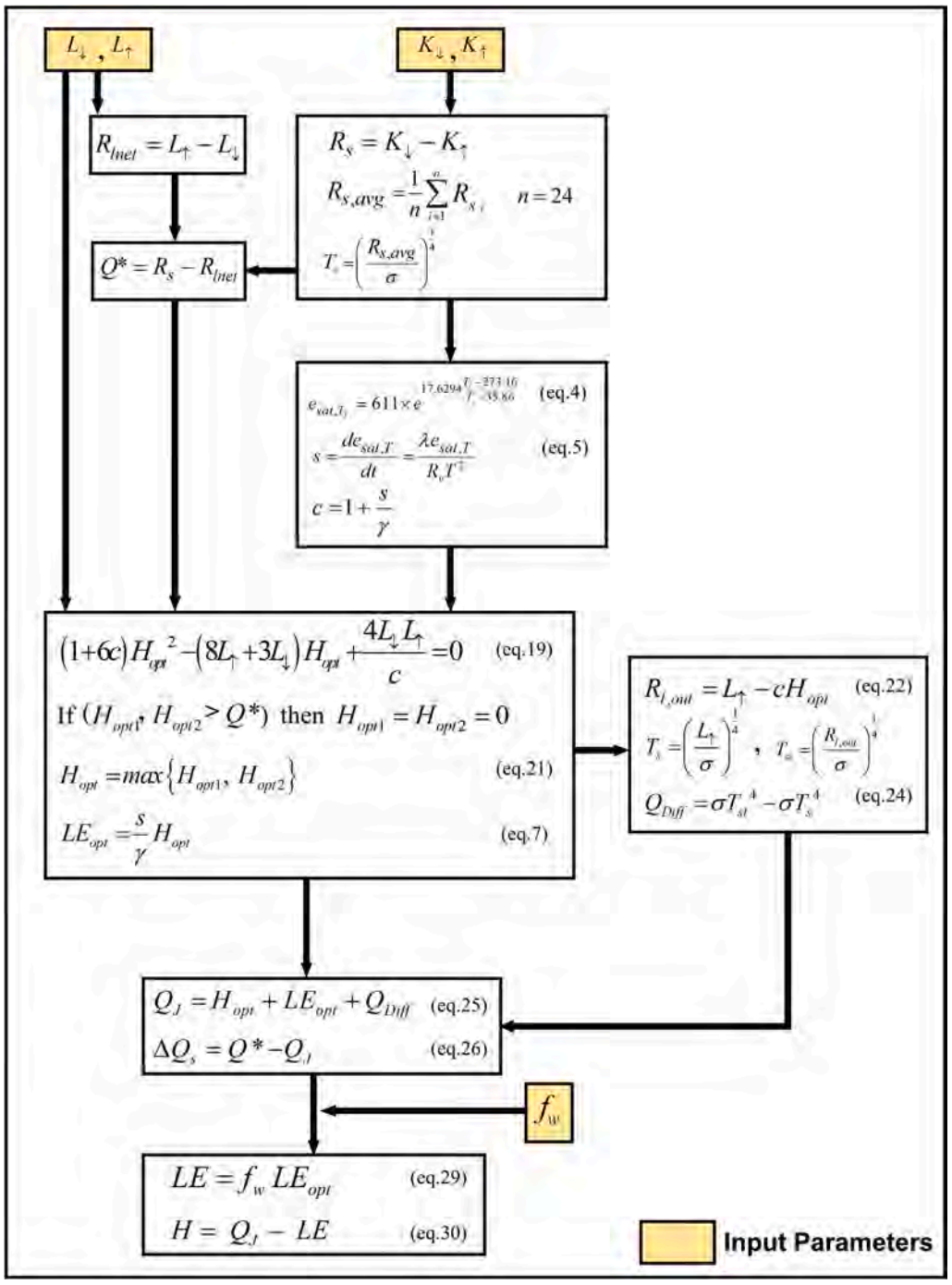

Fig. 2. Diagrammatic representation of the governing equations to estimate the land surface energy fluxes. The variables are explained in the main body and Appendix A.

$$LE = f_w\, LE_{opt} \tag{29}$$

$$H = Q_J - LE \tag{30}$$

3. Data and processing

3.1. Eddy covariance observations

To validate the developed theory, we used the FLUXNET2015 (Pastorello et al., 2020) database, which comprises in-situ observational data of turbulent flux and radiation components around the globe covering different climate zones and different land covers based on the IGBP classification. We also validated three urban regions limited to data availability. The FLUXNET2015 database comprises the eddy covariance observations of global sites and non-urban regions at 0.5 h resolution. We used 99 sites based on the availability of all radiation components, incoming and outgoing longwave and shortwave flux. Fig.3 depicts the location of EC sites colour coded with corresponding IGBP land cover. For validation with EC turbulent fluxes, the observed radiation data from the flux tower sites was used to estimate the total turbulent flux from the thermodynamic analytical solution ($Q_{Jthermo}$). For observed total turbulent flux ($Q_{JEC} = H + LE$), we used the sensible and the Latent heat flux not corrected for the surface energy balance closure. To ensure the data quality, we used the data points (0.5 h data) only for which

values of all the variables existed. We used total of 6617 site-months of all sites for the validation with a minimum of 12 months and a maximum of 180 months of a site from FLUXNET data. For urban regions, we used only three sites, JP-SAC in Sakai, Japan(25 months)(Ando and Ueyama, 2017), AZ-WPHX in Phoenix, Arizona(13 months)(Chow, 2017), and IN-VMCC in Mumbai, India(4 months)(Gupta et al., 2020) based on the availability of data with us.

3.2. Global satellite data

For global estimates and evaluation, we used four radiation variables (incoming shortwave, reflected shortwave, incoming longwave, and outgoing longwave radiation) at the surface level as satellite inputs from the CERES Edition4A SYN1deg-MHour product dataset(Rutan et al., 2015). The dataset is taken for the study period 2003–2019 and is at a spatial resolution of $1^\circ \times 1^\circ$ degree and a temporal resolution of monthly hourly. Further, we used the adjusted and all-sky conditions dataset to test the applicability at all climatic conditions. The surface radiation variables in SYN1deg products are computed based on Langley Fu-Liou radiative transfer model with inputs from the MODIS and CERES geostationary satellites (GEO), GEOS atmosphere and skin temperature, MATCH aerosol constituents, and MODIS spectral aerosol optical depths. The satellite instruments are calibrated against the MODIS data. Currently, the CERES EBAF dataset provides the most accurate top-of-atmosphere (TOA) radiation data over the land(Wild et al., 2015). The adjusted CERES Syn data used in this study was developed from the CERES EBAF Ed4.0-Surface fluxes derived from CERES EBAF TOA using the radiative transfer model. The Root mean square (RMS) difference of monthly mean Ed4.0 SYN1deg fluxes used here are similar to the RMS difference of monthly mean Ed4.0 EBAF-Surface fluxes. Uncertainties may exist in the surface values derived from the TOA fluxes (Kato et al., 2013) and are associated with clouds, aerosols, temperature retrievals, and parameterisation of radiative model.

To calculate the actual latent heat flux (LE) from the LE_{opt}, we obtained the evaporative stress factor (f_w) from the GLEAM v3.6b dataset, which has a monthly temporal resolution and 0.25° spatial resolution (Martens et al., 2017; Miralles et al., 2011). The f_w is based on vegetation optical depth and root zone soil moisture obtained using microwave remote sensing. We regridded the data to 1° resolution with first-order conservative mapping(Division and Alamos, 1999) using the Climate Data Operator (CDO) tool and assigned it to the flux grid as above.

To assess the global daytime variations, the hourly satellite data in UTC is converted to a single diurnal time cycle. Based on the local timezone of each grid, the time series in each grid is shifted to the corresponding diurnal time.

For surface energy flux assessments with global land cover, we extracted the IGBP-based land cover classification from the MODIS MCD12C1.006(Friedl and Sulla-Menashe, 2015) satellite dataset. We rescaled the 500 m resolution of MODIS to the 1-degree using the nearest neighbor algorithm. With total land cover classes of 16, we aggregated the classes to three major groups, Forests, Non-Forests, and Others, based on the canopy size. Further, the LC value from the upscaled data to the flux pixel was assigned based on the Nearest neighbor lookups of latitudes and longitudes.

3.3. Global land fluxes products

For spatial comparison, we used FLUXCOM (Jung et al., 2019), GLDAS-NOAH (Rodell et al., 2004), ERA5 monthly Reanalyses (Hersbach et al., 2020), GLEAM(Martens et al., 2017), and MODIS(Mu et al., 2007), depending on the availability of the variables. We identified a common period of 2001–2013 and a common spatial resolution of 1° depending on data availability. For our study, we used FLUXCOM RS + METEO 0.5° monthly averaged with uncorrected values for energy balance closure to assess with direct upscaling of EC observations. From the FLUXCOM ensemble, we compared our results with three machine learning products, Random Forests (RF), Multivariate Adaptive Regression Splines (MARS), and Artificial Neural Networks (ANN). The GLEAM 0.25° total monthly evaporation (mm) was converted to LE by adopting a constant latent heat of vaporization of 2.45 MJ mm^{-1}. The MODIS 16A2.006 at 8 day 500 m resolution LE (Running et al., 2017) was regridded similarly to MODIS LC. The FLUXCOM, ERA 5 reanalyses 0.25° at monthly averaged, and GLDAS NOAH 1° monthly were rescaled to 1° with first-order conservative mapping using CDO.

4. Results

4.1. Thermodynamic estimate of turbulent flux and its validation

4.1.1. In-situ point estimates for global sites

We first computed the thermodynamic estimate (TE) of turbulent flux calculated using the expressions (Equations19–25) (now denoted by $Q_{Jthermo}$) for flux sites, using four radiation components $K_{\downarrow}, K_{\uparrow}, L_{\downarrow}, L_{\uparrow}$. The radiation components were taken directly from the FLUXNET sites to estimate $Q_{Jthermo}$. We then compared $Q_{Jthermo}$ with the observed turbulent flux by eddy covariance (EC) technique (Q_{JEC}) at 102 sites (99 from FLUXNET and 3 urban regions) for which data of all radiation components and Q_{JEC} were available. We present the results for 38 sites with a minimum of 30 months of data (Fig.3, shown in map). For the urban regions, there are only 3 sites available, and we considered all of them. In Fig.S1, we have shown diurnal variation in T_{st} and T_s that leads to differential energy, which is corrected in the total turbulent convective energy (Eq. 24). In Fig.4, we present the average monthly diurnal variations of turbulent flux, comparing $Q_{Jthermo}$ and Q_{JEC}.

Fig.4 shows that turbulent heat flux thermodynamic estimates follow the diurnal variations depicted by the eddy covariance observations. The errors are minimal for the forest regions, Deciduous Broadleaf Forest (DBF), Evergreen Broadleaf Forest (EBF) and Evergreen Needleleaf Forest (ENF) [first 3 rows of Fig.4]. For the wetland (WET), at the site, US-WPT, the Q_{JEC} value is quite low compared to $Q_{Jthermo}$.Such a low value Q_{JEC} could be associated with measurement limitations, as the turbulent heat fluxes are normally high for wetlands due to high latent heat flux. The good resemblance between $Q_{Jthermo}$ and Q_{JEC} are observed in other WET sites in Fig.4. The plots for $Q_{Jthermo}$ and Q_{JEC} are very similar for cropland (CRO) and Savannas (SAV) (Fig.4). There are discrepancies for a few sites for grassland (GRA) and Open shrublands (OSH). The eddy-covariance observations at those sites show high closure terms; hence, there may be a possibility of measurement limitations. For urban regions (URB), there are differences, which may be because of urban structure that often introduces errors in Q_{JEC}. Overall, there is a very good match between $Q_{Jthermo}$ and Q_{JEC}, showing the efficacy of the thermodynamic model. The summary of RMSE (Root Mean Square Error) and MBE (Mean Bias error) of 102 sites is presented in Supplementary Table.S2.

Fig.5 presents the scatter plots of monthly values between $Q_{Jthermo}$ and Q_{JEC} at individual sites. For most sites for land use, DBF, EBF, ENF, WET and CRO, the points closely fall on the 45^0 lines with a very high R^2 value between $Q_{Jthermo}$ and Q_{JEC}. There are deviations for GRA, SAV, OSH and Urban sites, which are consistent with our observations from Fig.4. We regressed $Q_{Jthermo}$ against Q_{JEC} and presented the slope (m) and intercept (c) in Fig.5. For most cases, the slope is close to 1, and the intercept value is low, showing similarities between the thermodynamic estimates and on-site observations. Supplementary Table S2 summarizes the analysis of regression performances and coefficients (mean ± Standard Deviation (SD)) for all 102 sites. The adjusted R^2 value of 0.86 (Table.S2) shows good agreement between $Q_{Jthermo}$ and Q_{JEC}. The thermodynamic approach developed here is able to adequately explain the monthly variability of on-site turbulent heat flux observations. 56 out of 102 sites show R^2 values >0.9, and 82 sites >0.8. The slope and intercept describe the underestimations and overestimations by $Q_{Jthermo}$ with respect to Q_{JEC}.Overall, the analysis reveals slightly greater estimates of $Q_{Jthermo}$ for larger values of Q_{JEC} based on an average slope of 1.12.

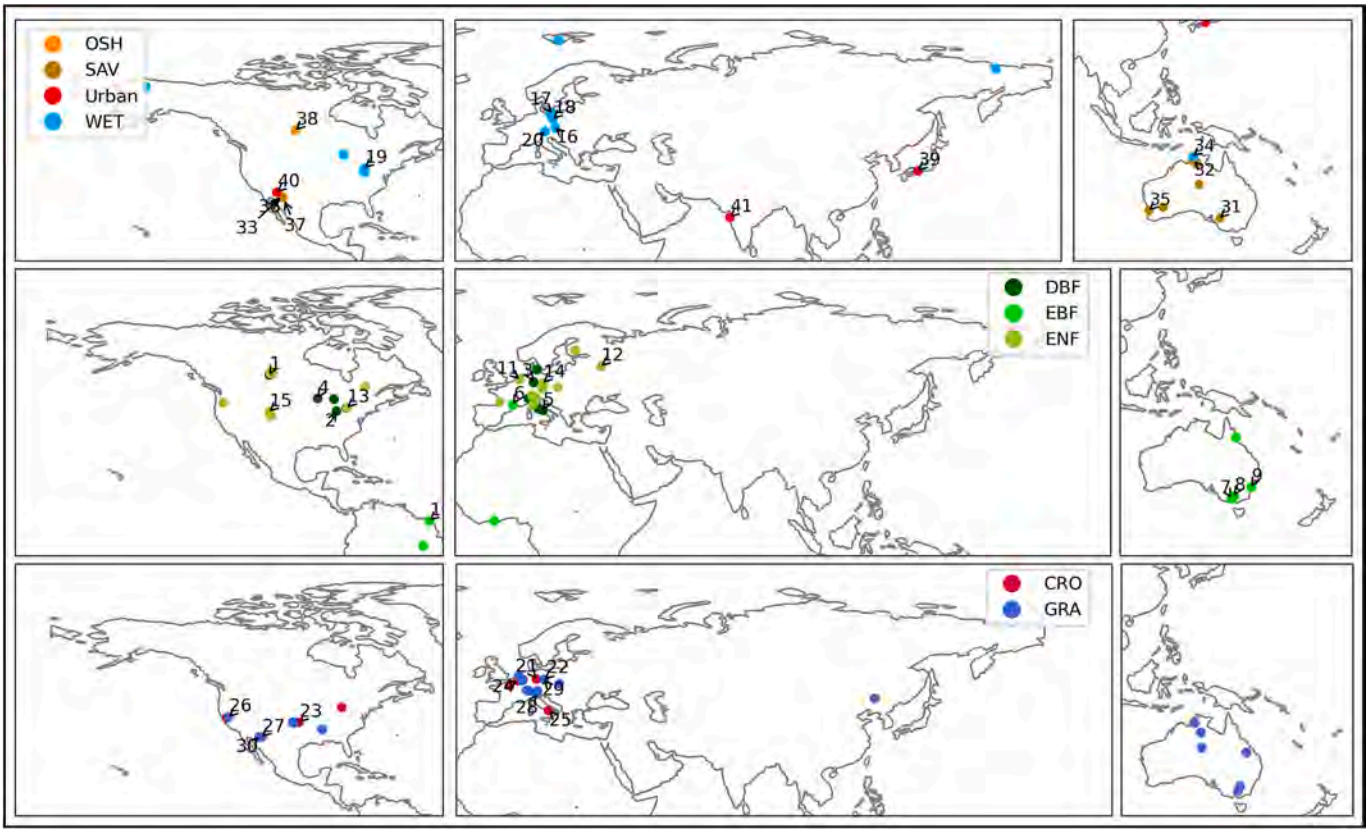

Fig. 3. The geographical locations of eddy covariance sites used for validation: Each dot represents an Eddy covariance location with colour code represents the associated land cover. The numbers are only assigned to the sites showed in the subsequent figures. The details of the sites based on the corresponding numbers can be accessed from the supplementary file TableS1. The study considers 9 LULC classifications. They are: DBF- Deciduous Broadleaf Forest, EBF- Evergreen Broadleaf Forest, ENF- Evergreen Needleleaf Forest, CRO- Croplands, GRA- Grasslands, SAV- Savannas, OSH- Open Shrublands, Urban, and WET- Wetlands.

Further, a low mean average intercept of 1.9 W m^{-2} indicates low bias for lower values. The discrepancies between the estimates $Q_{Jthermo}$ and Q_{JEC} indicate either the limitation of TE estimations or EC estimations, or both.

The detailed literature review (Mauder et al., 2020) of the past 25 years discussed the limitation of EC observations. They reported systematic underestimations of the turbulent energy due to uncertainties in the complicated data analysis in the EC technique. Further, the observations by a single flux tower are unable to capture larger-scale mesoscale eddy circulations. At almost all the flux tower sites, the surface energy balance does not follow the conservation of energy since the available energy (Q^*) is more than the sum of observed variables, Q_{JEC} and ΔQ_s measured by heat flux plate, resulting in residual energy (Q_{Res}). It could be possible that the TE estimates are overcoming the limitations of EC techniques; however, it is difficult to infer the same from the present analysis.

A detailed study (Stoy et al., 2013) based on the analysis of 173 FLUXNET sites concluded that the differences in the surface energy balance closure (C_{EB}), reciprocal to Q_{Res}, between different land covers (forests, non-forests, and other areas) are insignificant. However, the literature suggests that improvement in the C_{EB} is possible by addressing the underestimation of soil heat storage(Higgins, 2012) and considering unquantifiable factors, such as the role of water(Stoy et al., 2013), heat storage in the canopy(Heidkamp et al., 2018) and metabolic terms, as well as photosynthesis(Meyers and Hollinger, 2004). Further, a study (Lindroth et al., 2010) that assesses the energy balance closure showed that the heat flux from tree biomass, ignored in energy balance, is the biggest of the anticipated storage components in ΔQ_s. The case study (Heidkamp et al., 2018) of modeling turbulent fluxes for shallow vegetation showed improvement by including canopy heat storage elements. Thus, the Q_{Res} from EC estimation is also associated with underestimating ΔQ_s and should be dependent on the land cover types for obvious reasons. Further, as the Q_{Res}(C_{EB} is lower) is higher during daytime with higher Q^* (Franssen et al., 2010; Stoy et al., 2013), Fig.4 shows higher biases between the $Q_{Jthermo}$ and Q_{JEC}, during the daytime, which could be due to high Q_{Res}.

To understand the dependence of the bias on land cover, we present the relative differences in turbulent heat fluxes between $Q_{Jthermo}$ and Q_{JEC}, with respect to Q^*(scaled by Q^* for comparison) in Table.S3. The biases are computed for the peak daytime (10:00–14:30 local standard time). We applied the two-sample Kolmogorov-Smirnov two-sided test and k-sample Anderson-Darling test at a significance level of 0.05 to understand the differences between the bias samples from different land covers. We found that the scaled bias for forests (2.6 ± 13.5%) is significantly different from non-forests (includes GRA and CRO, 10.1 ± 8.7%), Wetlands (40.6 ± 64.2%), Urban areas (30.5 ± 1%), and Other areas (includes SAV and OSH, 13.3 ± 8.9%). Further, the individual differences are significant between non-forest & wetlands (WET), and Others and WET. Based on the monthly analysis, we found that the biases for the sites in non-forests (CRO and GRA) and Others (SAV and OSH) are highest in the precipitation months (Fig.S2). This bias is probably due to the limitations of EC stations in estimating high Latent Energy (LE). Thus, we conclude that $Q_{Jthermo}$ captures the limitation of Q_{JEC} to observe high turbulent energy, which occurs mainly in canopies with low biomass and heat storage elements. We found higher biases or additional turbulent flux compared to EC measurements for areas with low canopy elements (such as Non-forests) than areas with high canopy elements with more biomass (such as forests).

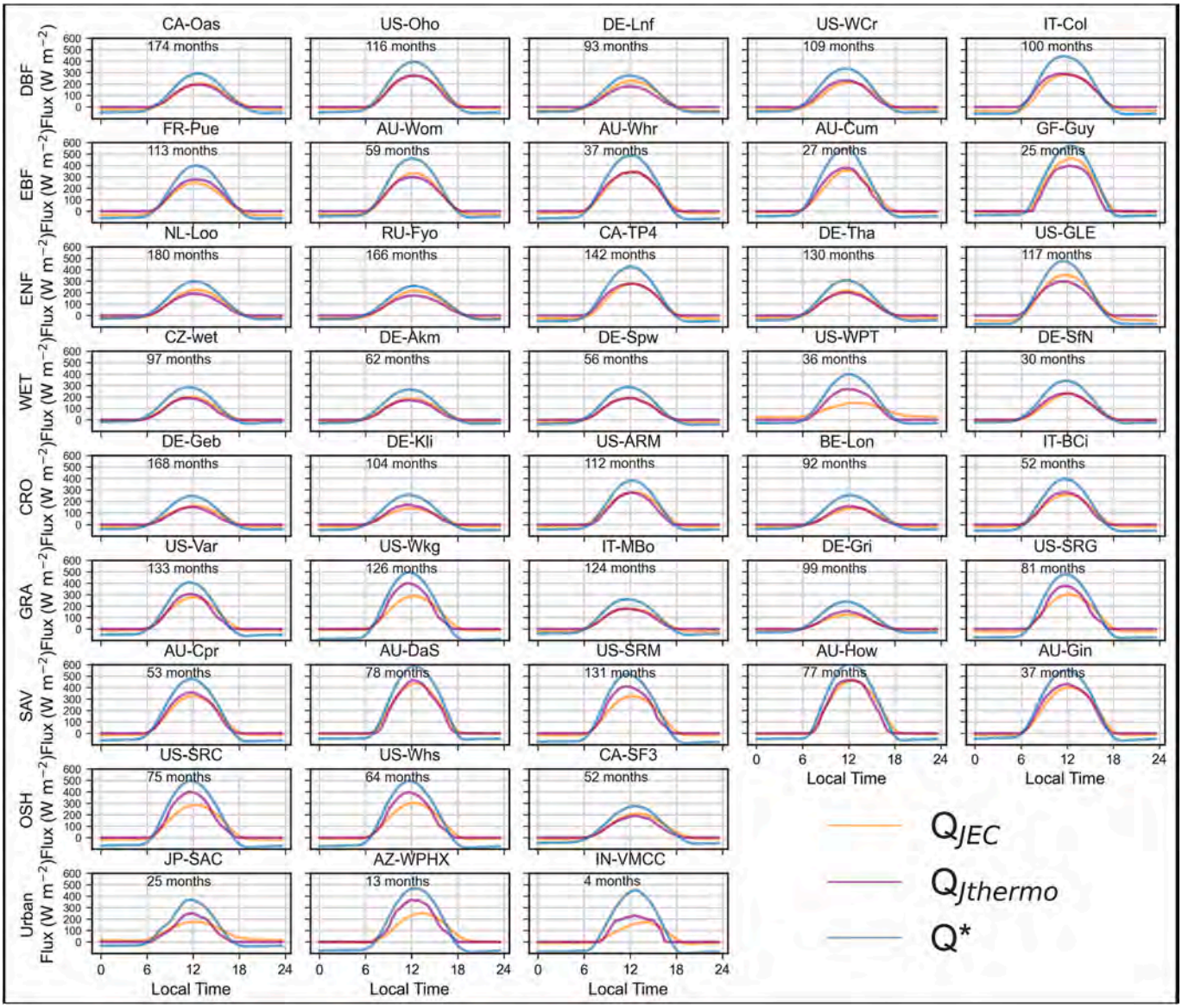

Fig. 4. Comparing the average diurnal variations of $Q_{Jthermo}$ and Q_{JEC}. The total turbulent flux from TE theory and EC observations is compared for 38 FLUXNET sites and three urban sites. The months in each box represents the averaging period for the respective site. They are arranged based on land covers: DBF Deciduous Broadleaf Forest, EBF- Evergreen Broadleaf Forest, ENF- Evergreen Needleleaf Forest, WET- Wetlands, CRO- Croplands, GRA- Grasslands, SAV- Savannas, OSH- Open Shrublands, and Urban. The locations of the sites are presented in Fig.3. Q_{JEC}, Observed turbulent heat flux by EC, $Q_{Jthermo}$ turbulent heat flux estimated from the thermodynamic model, Q^* - Observed net radiation.

4.1.2. Global estimates of turbulent heat fluxes and their validation with EC observations

After validating our methodology, we used it to develop globally distributed land surface estimates of turbulent fluxes at 1° spatial resolution using four radiation variables, all-sky incoming and outgoing shortwave, and longwave radiation flux ($K_{\downarrow}, K_{\uparrow}, L_{\downarrow}, L_{\uparrow}$), at the surface level obtained from the remotely sensed dataset CERES Edition4A SYN1deg-MHour, which is at a spatial resolution of 1° and temporal resolution of monthly hourly. We present the results in Fig.6. The figure shows the spatial variations of the radiation components at the surface for four seasons, DJF, MAM, JJA, and SON. The period considered is 2003–2019. The globally distributed land surface Net radiation (Q^*) (Fig.6, top row) estimated from the incoming and outgoing fluxes, is used to calculate the global turbulent heat flux field (Q_J)(Fig.6, 2nd row) based on thermodynamic principles using the expressions (19–25). Fig.6, 3rd row presents the land surface storage heat flux (ΔQ_S). The major parts of the northern hemisphere have the highest positive value of (ΔQ_S) in JJA, followed by MAM, which steadily becomes negative in SON and the highest negative during DJF. This is expected due to seasonal patterns. However, we found positive ΔQ_S throughout all the seasons for Amazon forests and Middle Eastern Africa characterized by mostly Tropical and Subtropical moist climates with moist broadleaf forests, grasslands, savannas and shrublands. We further calculated the global latent and sensible heat flux fields (Fig.6, last two rows) using eqs. 27–30 and f_w. During the JJA season, the monsoon regions north of the Equator, such as South Asia, have a high latent heat flux due to the wet season. The desert/arid regions, like Sahara in Africa or California in the US, have low latent heat flux, resulting in very high sensible heat flux. The radiation components are generally lowest in the northern hemisphere in DJF due to seasonally low Q^*.

We validated our estimates using remote sensing data with the flux tower estimates. We picked up the site with the highest data points for validation for each land cover. We see the monthly variation between CERES and FLUXNET by assessing variation for absolute magnitude

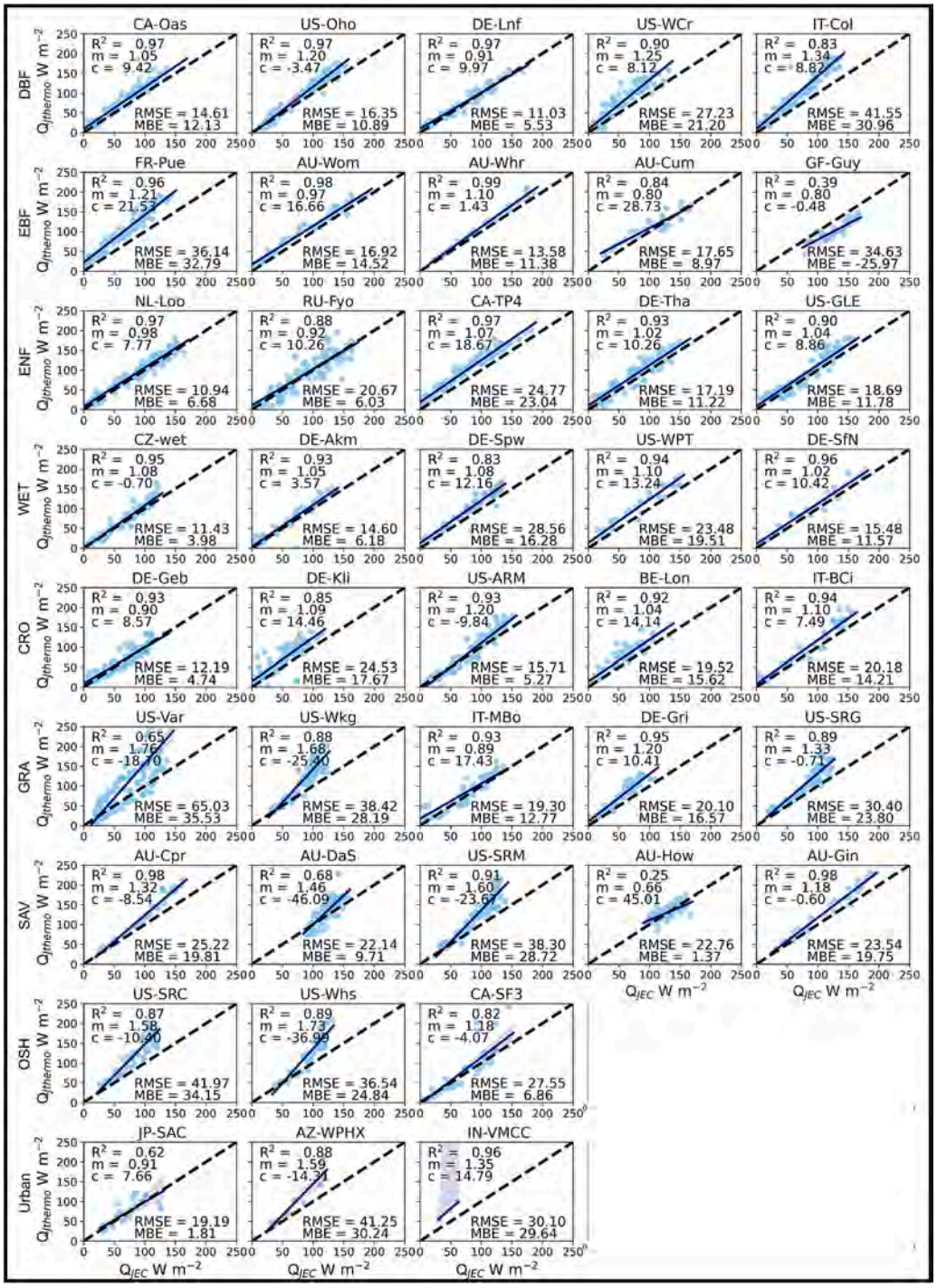

Fig. 5. Evaluating the $Q_{Jthermo}$ with Q_{JEC} using correlation statistics. The data points are at the monthly averaged. The adjusted R^2 is the explained variance of $Q_{Jthermo}$ by Q_{JEC} and a measure of the fit; slope (m); and intercept (c) are the regression coefficients. Root mean square error (RMSE) and Mean Bias error (MBE) are estimated for $Q_{Jthermo}$ with respect to Q_{JEC}.

(Fig.7) and monthly anomalies after deseasonalization (Fig.S3). For absolute values, we have found a very strong similarity. The results depict high agreement in the variables, $K_{\downarrow}, L_{\downarrow}$ and $L_{\uparrow}$ of CERES and FLUXNET 2015 in-situ dataset with adjusted R^2 values >0.96 for all the sites. However, we observe an underestimation of $K_{\uparrow}$ from CERES for a few sites. The $Q_{Jthermo}$ estimated from these input variables from CERES shows high agreement with an adjusted R^2 >92%. The scatter plots between thermodynamic estimates from satellites and in-situ observations show all the points falling close to the 45^0 line. For monthly anomalies, the CERES shows good agreement for $K_{\downarrow}, L_{\downarrow}$ and $L_{\uparrow}$ to FLUXNET but less as compared to the absolute values. The $K_{\uparrow}$ shows less agreement as it depends on land surface characteristics like albedo and land use, which differs due to scaling challenges while linking remote sensing footprints to tower footprints. Further, the estimated $Q_{Jthermo}$ from CERES matches well (with average adjusted R^2 = 0.6) with the FLUXNET sites observations. Thus, we see the capability of the analytical thermodynamic-based expressions to estimate the global surface fluxes.

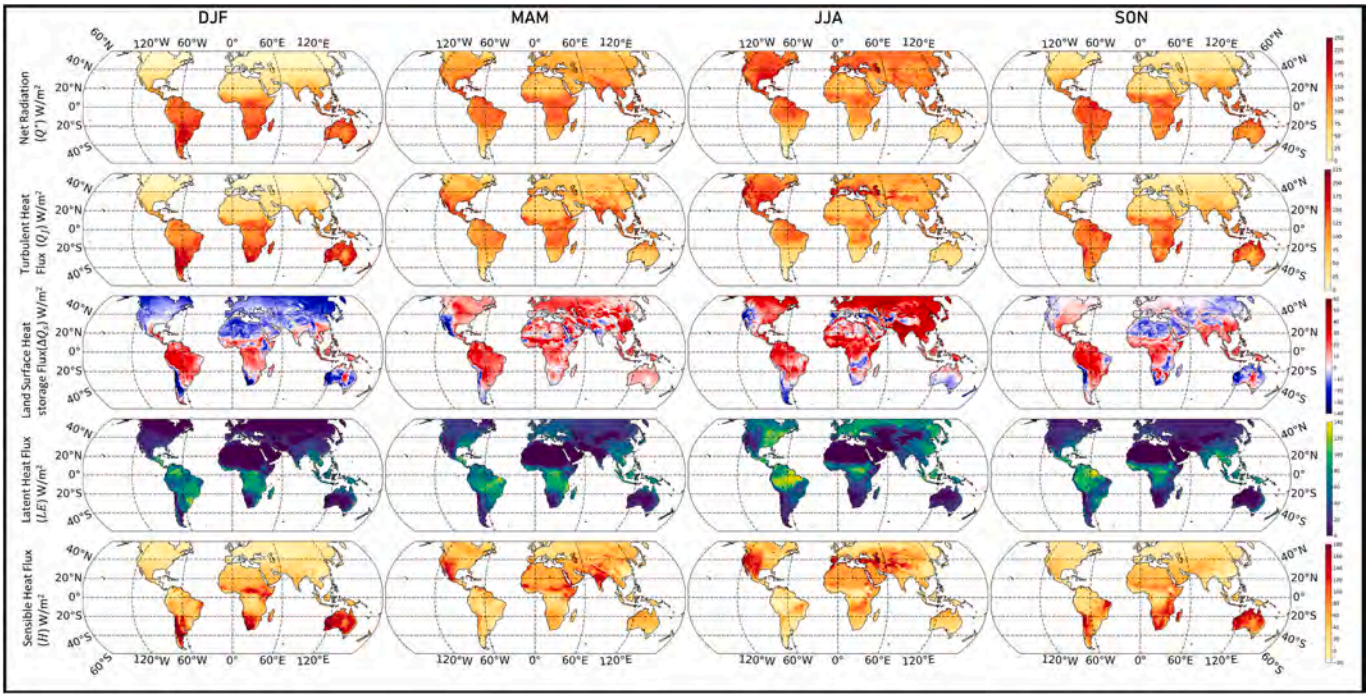

Fig. 6. Seasonal variation of estimated annual average fluxes for the period 2003–2019. The fluxes are estimated from the CERES monthly global Syn dataset at 1° resolution. Q^*(Net Radiation) derived from CERES radiation components ($K_\downarrow$, $K_\uparrow$, $L_\downarrow$, $L_\uparrow$). Q_J (Turbulent heat flux) and ΔQ_S(land surface heat storage) are the estimated fluxes from the thermodynamic model. The global latent heat (*LE*) and Sensible heat (*H*) flux fields are estimated based on the evaporative stress factor from the GLEAM dataset.

4.1.3. Validation with global products of land fluxes

We compared the analytical estimates of global spatial patterns of mean annual Q_J with FLUXCOM, GLDAS, and ERA5 Reanalyses. For *LE*, we compared with FLUXCOM, GLEAM, and MODIS. The comparison (Figs. 8 and 9) shows the large global patterns of Q_J and *LE* consistent in all products. The Q_J is observed to be high in the tropical regions due to high incoming radiation as compared to the high latitude regions with low incoming radiation. The *LE* shows higher values, especially, regions of global monsoon domains, such as South American Amazon region, middle Africa, Asian region with India and south-eastern China, and North Australia. Among the FLUXCOM ensembles, $Q_{Jthermo}$ performs best with fluxes from the random forest (RF) algorithm (shown in Fig7. Second row) with highest coefficient of variation (R^2 = 0.82) and regression slope (m = 0.95) as compared to MARS (R^2 = 0.76, m = 0.88) and ANN (R^2 = 0.79, m = 0.67) (Fig.S4). $Q_{Jthermo}$ performs almost similarly in MARS and RF, but comparison with ANN shows higher negative bias especially in regions of global monsoon domains, like Amazon forests, middle Africa, and east Asia (Fig.S4). On estimating the residual heat flux (Q_{Res}), the ANN shows high negative values (Fig.S5) in the same regions which should be due to overestimation of Q_J and explains higher negative bias with $Q_{Jthermo}$. With RF and MARS, $Q_{Jthermo}$ shows positive bias in most regions like the EC observations. As discussed in the section 4.1.1, such bias could be due to EC limitations to observe all turbulent energy and percolates in the FLUXCOM RF and MARS from uncorrected observed EC fluxes. The evaluation of $Q_{Jthermo}$ with Noah Land surface model (LSM) based GLDAS product depicts best agreement (Fig.8, third row) with high R^2 (R^2 = 0.91) and least bias (−0.51 Wm^{-2}) and RMSE(11.52 Wm^{-2}). In many LSMs such as Noah (Niu et al., 2011), the residual energy for energy balance closure is inherently assumed only to heat the soil column. The negative bias in $Q_{Jthermo}$ or higher values of Q_{JGLDAS} in high canopy areas of tropical regions, such as Amazon rainforests and middle Africa, may be associated with excessive soil heating due to the residual energy in the model. The increased surface temperature drives the turbulent heat, which otherwise would be trapped as a canopy heat storage within the canopy. This is reflected in the limitations of the models to capture the nighttime warming by the forests that dampen the diurnal temperature range (Meier et al., 2018, 2019; Schultz et al., 2017). Compared with ERA5 (Fig.8, fourth row) reanalyses, $Q_{Jthermo}$ performs well but shows higher values (positive bias) for low Q_{JERA}. The Q^* from CERES is higher than the Q^* from ERA5 (Fig.S6) in the same regions. The underestimation of Q^* in ERA5 could be the reason for lower Q_{JERA} or higher $Q_{Jthermo}$ in these regions.

Using f_w from GLEAM to estimate *LE* provided excellent agreement (R^2 = 0.93, m = 0.87) with GLEAM for obvious reasons; however, it could result in underestimation as the stress factor will proportionally decrease the interception evaporation from LE_{opt}. This is observed in Fig.9, second row, where the LE_{thermo} shows lower values than LE_{GLEAM} in Amazon forests, middle Africa, and east Asia. LE_{thermo} shows higher values in other regions, possibly due to higher potential evaporation estimates LE_{opt} at equilibrium partitioning than from GLEAM, as both products use the same CERES Net radiation data. The other reasons could be the assumptions of soil heat flux to be a constant fraction of Q^* in GLEAM and the use of homogenous plant functional type. This underestimates LE, as depicted by Zimba et al. (2022). With FLUXCOM RF, LE_{thermo} agrees well (Fig.9, first row, R^2 = 0.80, m = 1.08) but shows higher values in monsoon-rich regions and high latitudes, possibly due to the underestimation of upscaled uncorrected EC values in $LE_{FLUXCOM}$. In comparison with MODIS (Fig.9, third row), LE_{thermo} agrees adequately (R^2 = 0.80, m = 0.87) and performed best in dense forest regions such as Amazon, central west Africa, boreal forests, and southeast Asia. LE_{thermo} shows positive bias in regions with low and moderate *LE* such as India, north of central Africa, and southern part of South America. The evaluation of global terrestrial evaporation data sets using EC towers by the WACMOS-ET project shows that the MODIS evaporation underestimates LE in the tropics and subtropics compared to other products such as GLEAM(Miralles et al., 2016). Such underestimation by MODIS evaporation products is also reflected in the performance measures of our products with different datasets (Fig.9).

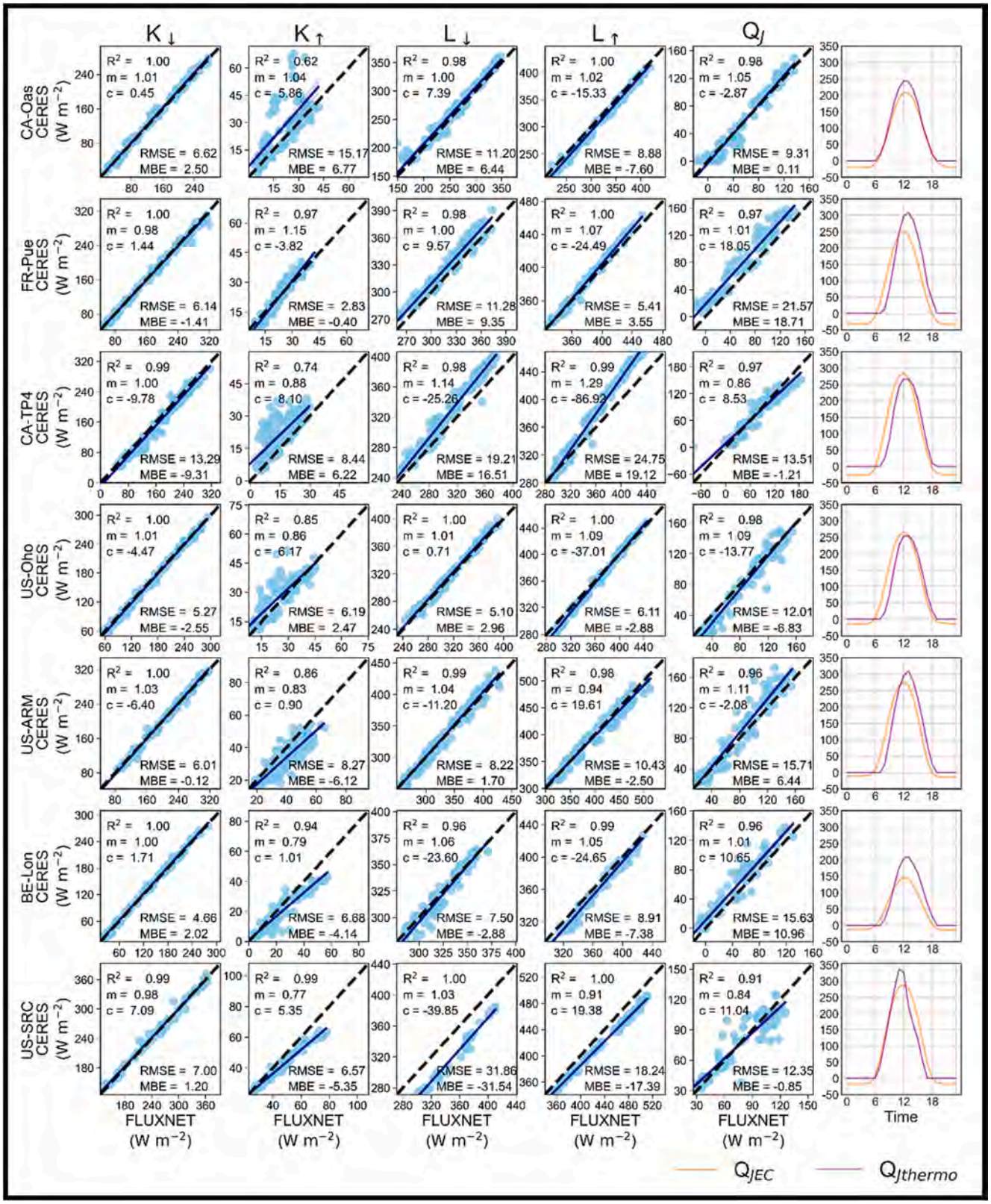

Fig. 7. Validation of $Q_{Jthermo}$ derived from CERES. The monthly estimates of $Q_{Jthermo}$(turbulent heat flux estimated from the thermodynamic model with inputs of radiation variables from CERES monthly global Syn dataset at 1° resolution) with Q_{JEC} (Observed turbulent heat flux by EC from FLUXNET2015 databases). The figure also shows the variation of CERES Incoming shortwave radiation ($K_{\downarrow}$), Outgoing shortwave radiation ($K_{\uparrow}$), Incoming longwave radiation ($L_{\downarrow}$), Outgoing longwave radiation ($L_{\uparrow}$) with observed on-site data of corresponding variables on flux towers within the grid. The statistics used are very similar to Fig.5.

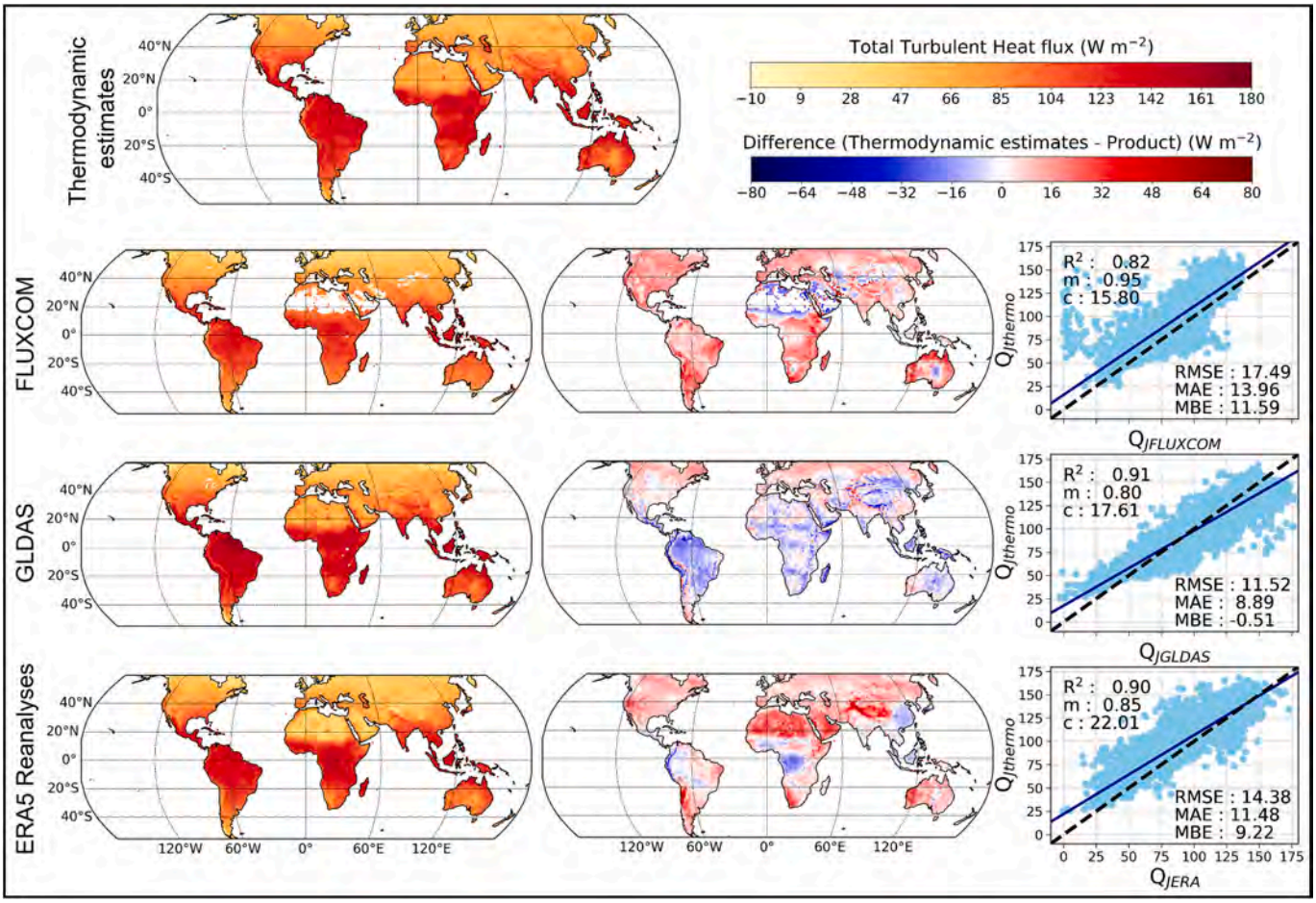

Fig. 8. Spatial validation of Q_J derived from CERES with global products. The mean annual estimates of Q_J are compared. The first row depicts the spatial Q_J from thermodynamic estimates. From second row, the first column is the global values of Q_J from global products, the second column depicts the bias ($Q_{Jthermo}$ - $Q_{Jproduct}$) between thermodynamic estimate and global products, the last column is the evaluation of spatial values of $Q_{Jthermo}$ with $Q_{Jproduct}$ using correlation statistics and regression coefficients. RMSE, MAE, and MBE have units Wm^{-2}.

4.2. Thermodynamic estimate of global land surface heat storage

The land surface heat storage flux (ΔQ_s) is defined as the net heat storage change (uptake or release) in the volume per unit of horizontal land area. The land volume comprises a certain depth of the ground and the canopy elements associated with land covers such as buildings and vegetation in urban areas and biomass of trees in forests(Oke and Cleugh, 1987). Here, we present the first global estimates of ΔQ_s as energy balance residual using eq. 1 with Q_J as $Q_{Jthermo}$ and analyze its behaviour geographically. In general, ΔQ_s is minimal in wet areas with sparse canopy elements due to high *LE* but reaches a higher value in arid regions with values equivalent to *H* and often exceeds *LE*. Further,ΔQ_s with a considerable amount of biomass heat storage in forest regions dampens the diurnal temperature range(Meier et al., 2019). We examine these behaviours of ΔQ_s on global land by estimating daily means (Fig.10, column 1) and daytime means (10:00 to 14:30 local time, Fig.10, column 2) for 2003–2019 to see if these processes are accurately represented. The arid regions such as mainly in the southwestern United States, the Sahara Desert in northern Africa, the Arabian Peninsula, the Thar desert in India, and central Australia have a very high positive ΔQ_s (Fig.10c) and $\Delta Q_s/Q^*$ (Fig.10d) during the peak solar hours because of low *LE*. However, in the non-peak solar hours the land surface in these regions releases much heat, resulting in very low to negative 24 h mean values of ΔQ_s (Fig.10 a) and $\Delta Q_s/Q^*$ (Fig.10 b). The mean daily ΔQ_s and $\Delta Q_s/Q^*$ show a substantial amount of energy throughout the Amazon forests compared to barren regions like the Sahara Desert. This characteristic is due to the heat storage capacity of the biomass. However, during the peak solar hours, high evapotranspiration and high *LE* results in a comparatively low land heat storage flux, as compared to the arid regions. Further, we see that the percentage $\Delta Q_s/Q^*$ is highest in the arctic-boreal regions (Fig.10c) during both daily and daytime mean as permafrost acts as a large sink of energy and net radiation melts ice in the active layer(Engstrom et al., 2006). However, ΔQ_s during peak solar hours shows smaller values than arid regions due to the low net radiation (Fig.10d).

4.3. Global average land fluxes estimates and comparison with literature

With an absorbed land-mean solar radiation of 143 Wm^{-2} at the surface and net longwave emitted from the land surface given by 59 Wm^{-2}, we estimate the global land (90°N-90°S) Q^* of 84 Wm^{-2} for 2003–2019 (Table.S4) based on the CERES Syn dataset. The estimate is similar to the CERES EBAF Q^* of 79.10 Wm^{-2} calculated for the same period. Our estimates are slightly higher than the estimated Q^* values of 77.5 Wm^{-2} by Jung et al. (2019), 76 Wm^{-2} by L'Ecuyer et al., (2015), and 70 Wm^{-2} Wild et al. (2015). Based on the Q^* as input from CERES Syn, the thermodynamic model estimates global land Q_J as 82 Wm^{-2} and ΔQ_s as 2 Wm^{-2}. All the global value in this study are determined as area-weighted average over the land. The global *LE* is 40 Wm^{-2}. The value is consistent and in good agreements with 39.5 W m^{-2} by Jung et al. (2019), 38.5 W m^{-2} by Trenberth et al. (2009), 37–59 W m^{-2} by Jiménez et al. (2011), and 38 W m^{-2} by Wild et al. (2015). For the same

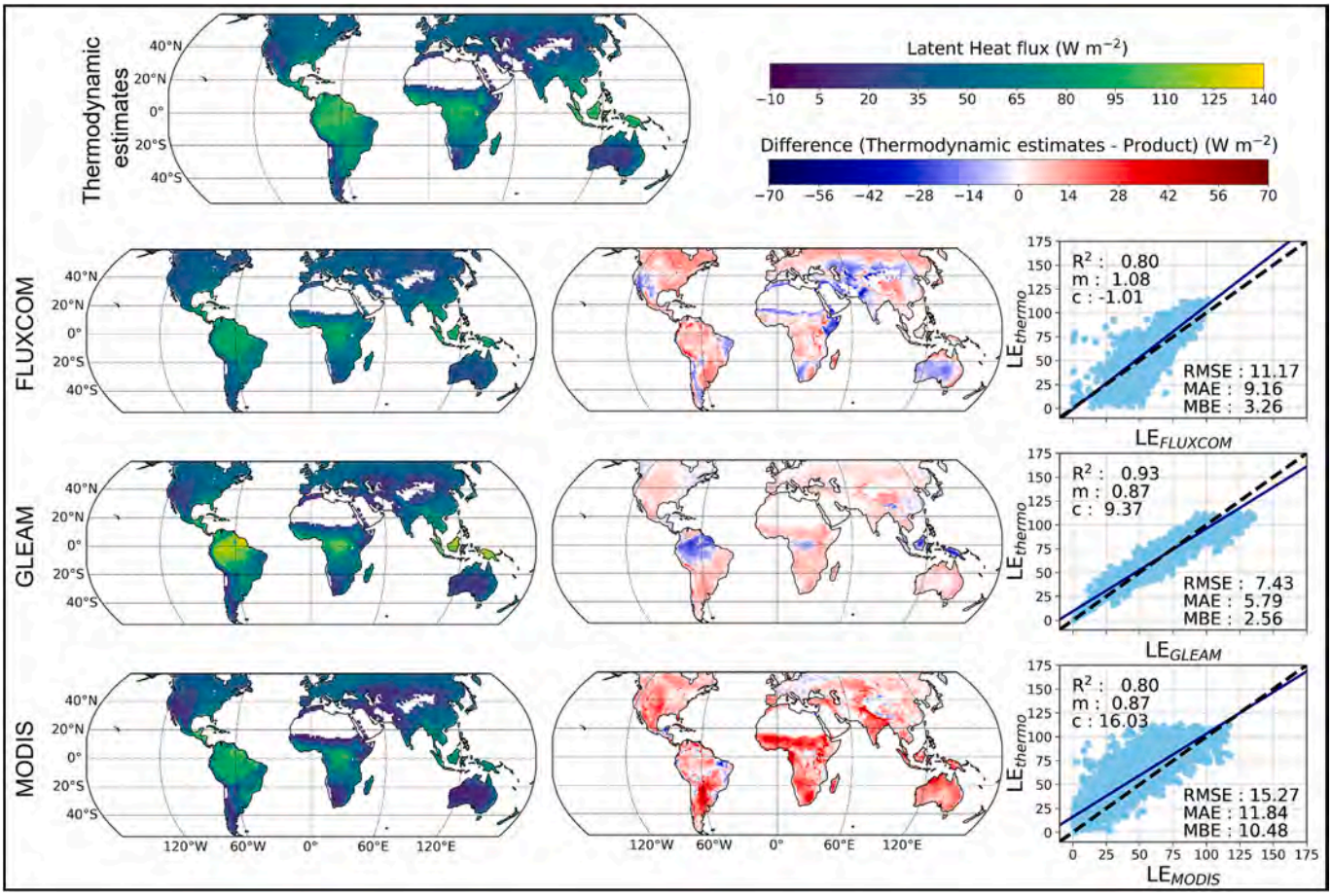

Fig. 9. Spatial validation of *LE* derived from CERES with global products. The mean annual estimates of *LE* are compared. The first row depicts the spatial *LE* from thermodynamic estimates. From second row, the first column is the global values of *LE* from global products, the second column depicts the bias ($LE_{thermo} - LE_{product}$) between thermodynamic estimate and global products, the last column is the evaluation of spatial values of LE_{thermo} with $LE_{product}$ using correlation statistics and regression coefficients. RMSE, MAE, and MBE have units Wm^{-2}.

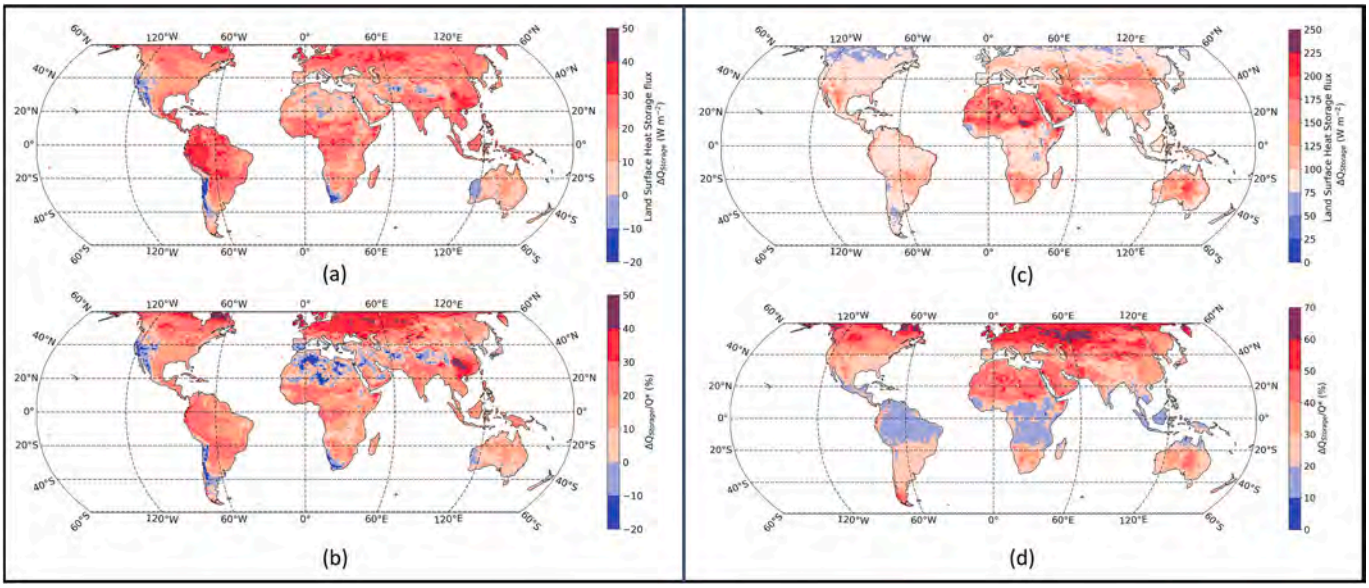

Fig. 10. Global estimates of land surface heat storage and its variation as global average and daytime average. The heat storage flux is estimated using the thermodynamic theory derived in this study. Column 1 depicts the daily means of (a) Land surface heat storage flux ΔQ_s and (b) ΔQ_s scaled by $Q^*(\Delta Q_s/Q^*)$. Column 2 depicts the same variables (c) ΔQ_s and (d) $\Delta Q_s/Q^*$ but averaged over local daytime (10:00–14:30 HRS).

global spatial extent global H, as the difference between Q_J and LE, is 42 W m^{-2}. The estimated H is in excellent agreement with Jung et al. (2011) with the value of 41 ± 4 Wm^{-2}, higher than the range of 36–40 W m^{-2} estimated by Siemann et al. (2018), lies well above 27 W m^{-2} estimated by Trenberth et al. (2009), and well within the range of 18–57 W m^{-2} estimated by Jiménez et al. (2011).

We found that the land use land cover drives the distribution of land surface heat fluxes (Table.S4). For example, the forest regions have a high value of global area averaged ΔQ_s for the period 2003–2019 as 6.72 Wm^{-2}.This is because of high canopy heat storage potential. On the contrary, the non-forest regions have a globally averaged ΔQ_s as 2.7 Wm^{-2}. The same is true for shrublands and Savannas with average value of 1.5 Wm^{-2}. The barren regions have negative values of −2.47 Wm^{-2} for ΔQ_s. The distributions show the role of vegetation in storing heat fluxes and thus driving the partitioning of incoming radiation fluxes perturbing local climate. The differential values of ΔQ_s across land use land covers are consistent with previous literature on parametrized models for heat storage(Meier et al., 2019).

5. Discussions

Our analytical approach for estimating surface energy fluxes is based on updating the previous theory that describes the land-atmospheric interactions as a radiative-convective system with energy and entropy budgets using the first and the second law of thermodynamics, respectively. The approach draws on the interplay between two parallel cooling mechanisms of the land, net longwave radiative exchange and turbulent cooling, after getting heated up by solar radiation. The turbulent flux develops due to local buoyancy generation and the power to drive convection, which is analogous to the working of a heat engine. We proposed that the Carnot limit, which is the maximum efficiency of a heat engine to produce power, should apply only to the sensible heat flux-driven dry convection near the land. Further, due to the land-atmosphere being a dissipative system, we added one extra constraint in which heat released due to the frictional dissipation of mechanical energy of air parcel becomes the internal energy of the atmosphere.

The importance of this approach lies in estimating non-radiative fluxes, Q_J and ΔQ_s, of surface energy balance with only four radiative inputs without any parameterization. Since radiative information can be retrieved from remote sensing, the approach being independent of surface and climate characteristics inherently captures the variability associated with heterogeneity otherwise constituted as parametrization and constants with only broad classifications in RS models and LSMs. Further, this allows the method to be computationally efficient for global application.

Our results compare well with the EC observations, signifying that the additional constraints imposed by thermodynamics perform well in providing the analytical solution in land-atmospheric interactions. We also explored the cases of disagreements, and while doing so, we could address some of the unresolved science questions, such as the distribution of residual energy in the land surface energy balance, limitations of EC observations, and the role of land surface heat storage (Mauder et al., 2020; Stoy et al., 2013). As Q^* in the energy balance equation, partition only into Q_J and ΔQ_s, a clear definition of ΔQ_s should be consistent with all land covers. Studies showed the importance of canopy heat storage in altering local climate (Meier et al., 2018, 2019; Schultz et al., 2017) and parameterized to several land surface models for non-urban spaces like forests (Boone et al., 2017; Heidkamp et al., 2018; Moore and Fisch, 1986). Rather than considering the canopy heat storage as an additional term, we followed the definition of ΔQ_s by (Oke and Cleugh, 1987) that comprises heat storage in all components of the canopy, including sensible and latent heat storage and ground (soil in non-urban areas). In the results, firstly, the higher mean $Q_{Jthermo}$ than observed Q_{JEC} suggests that $Q_{Jthermo}$ has overcome the limitation of EC in estimating the entire turbulent energy. Secondly, our results demarcated the impact of land covers in partitioning to Q_J and ΔQ_s, which were not apparent with EC observations. Our findings suggest that the land surface with dense canopy, high biomass, and wet regions tends to have high ΔQ_s as compared to the vegetation of lower canopy due to the buffering effects of the canopy. In the arid regions with a very low canopy, like Sahara Desert and Arabian Peninsula, the higher values of ΔQ_s during the day indicates the absence of latent heat flux and subsequent cooling by net longwave radiation from the land surface. The lower daily mean (including both day and night) ΔQ_s in these regions indicates the negligible buffering capacity.

Our results on validation with global products show great agreement in the spatial distribution of the fluxes. When compared with FLUXCOM products, we found that the performance of our approach is sensitive to the ML algorithms used in FLUXCOM. The level of agreement was in the order of RF > MARS>ANN in FLUXCOM ensemble. Like the EC comparison, the higher estimation of total turbulent flux than FLUXCOM depicts the improved outcomes. The best performance with the GLDAS suggests the importance of data assimilation in LSMs to estimate fluxes. The ERA5 reanalysis shows a lower value of Q_J due to the underestimation of Q^*.

Although radiative inputs from CERES Syn monthly dataset used here are based on accurate CERES EBAF TOA, there is a possibility of high uncertainty in the input. For a global observed land Net radiation (Q^*) of 84 Wm^{-2} from the satellite, we found the long term (2003–2019) average value of H,LE and ΔQ_s to be 42 Wm^{-2}, 40 Wm^{-2} and 2 Wm^{-2}, respectively. The H and LE are in great agreement with the literature. However, the long-term mean ΔQ_s is found to be higher. The average of land and ocean long term surface heat flux should not be >1 Wm^{-2}, which corresponds to earth energy imbalance(Schuckmann et al., 2020). In our model, we could not address this uncertainty, which is a caveat of our approach.

For partitioning total turbulent heat flux, our approach offers another advantage by using the microwave remotely sensed evaporative stress factor (f_w) spatially available for each grid. In comparison to FLUXCOM and MODIS, the LE estimates show higher values. However, we used f_w from GLEAM dataset, which does not consider interception evaporation. This is another limitation of our study.

Despite these limitations, our approach has plenty of potential applications for assessing surface energy budget in a changing climate and land use. We believe that the present work provides the first step to simulate land surface fluxes solely based on physical principles without parametrization.

6. Conclusions

We developed an analytical approach to estimate turbulent and land surface heat storage fluxes based on the thermodynamic principles of maximum convective power. Working on the previous studies on the thermodynamic theory that describes the land-atmosphere as a radiative-convective system, we improved the theory to estimate the turbulent fluxes successfully. The uniqueness of the approach is that this needs only incoming and outgoing surface radiation fluxes that are merged satellite and model products. The methodology is validated against the flux tower observations across the globe from different land use land covers. For the first time, such a method provides globally gridded analytical estimates of turbulent and land surface storage heat fluxes without using climate or land surface models involving parameterizations, thus not suffering from model deficiencies and uncertainties. We found that such thermodynamic estimates also overcome some of the limitations of the eddy covariance estimates. We further analyzed the spatial and diurnal variations of the turbulent and land surface heat storage fluxes and found them consistent with our existing site-specific knowledge. The spatial estimates agreed well with the global land surface flux products. The methodology is applicable to in-situ observation sites as well as to a large region. The surface energy products generated through the present study overcome the limitations of the non-existence

of observed surface energy flux data and will help the climate community understand the trajectory of surface processes across land use changes in a warming environment.

Funding

The authors would like to thank the Ministry of Human Resource Development (MHRD), Government of India for funding this study under the grant titled Frontier Areas of Science and Technology (FAST), Centre of Excellence in Urban Science and Engineering (Grant Number 14MHRD005). The work is financially supported by the Department of Science and Technology Swarnajayanti Fellowship Scheme, through project no. DST/ SJF/ E&ASA-01/2018-19; SB/SJF/2019-20/11, and Strategic Programs, Large Initiatives and Coordinated Action Enabler (SPLICE) and Climate Change Program through project no. DST/CCP/CoE/140/2018.

Author contributions

SG and MG conceived the idea and designed the problem. MG developed the theory and derived the analytical framework. MG and SG applied the theory and analyzed the results. MW reviewed the results and provided suggestions for improvements. MG and SG wrote the manuscript. MW reviewed the manuscript.

Declaration of Competing Interest

The authors declare that they have no competing interests.

Data availability

The FLUXNET2015 data used in the study are available at https://fluxnet.org/data/fluxnet2015-dataset/ (doi: https://doi.org/10.1038/s41597-020-0534-3). The CERES Edition4A SYN1deg-MHour product is available from https://ceres.larc.nasa.gov/data/. MODIS MCD12C1.00664 dataset for IGBP global land covers can be accessed at https://lpdaac.usgs.gov/products/mcd12c1v006/ (doi: https://doi.org/10.5067/MODIS/MCD12C1.006). The GLEAM v3.6b dataset can be accessed from the https://www.gleam.eu/.

Acknowledgments

SG acknowledges Sonia Seneviratne of ETH, Zurich, and Vishal Dixit of IIT Bombay for technical discussions.

Appendix A. Atmosphere as a convective dissipative heat engine

The radiative heating of the surface makes the air parcel in contact gain a lower density, increase its potential energy, and develop a state of thermodynamic disequilibrium. This disequilibrium causes the system to derive work as a heat engine to generate a convective motion by creating a buoyant force to reduce the potential energy of the parcel and depletes the temperature gradient. This motion is associated with transporting energy, mass, and momentum through fluxes between the surface and the atmosphere.

A.1. Carnot limit of a heat engine

Consider a heat engine with two reservoirs, a hot reservoir and a cold reservoir, and heat fluxes from the hot reservoir as J_{in} and comes out from the cold reservoir as J_{out}. In the case of the land-surface atmospheric convective system similar heat engine develops such that the hot reservoir is the surface, a source of turbulent fluxes J_{in}, with a temperature T_s. The cold reservoir is at the boundary of the atmosphere, where the effect of local convection merges with large-scale motion, and the engine releases heat J_{out} from the local convective system at a radiative temperature T_r.The engine develops a power $G = dW/dt$, work per unit time, that generates convective motion using turbulent heat as input from the surface. For maximum Carnot power and efficiency, no heat is used to increase the engine's internal energy, and the heat input is fully utilized to generate power.

The energy balance is expressed as:

$$J_{in} = J_{out} + G \tag{A1}$$

The entropy balance of the engine with internal entropy generation (σ) is:

$$\sigma + \left(\frac{J_{in}}{T_s} - \frac{J_{out}}{T_r}\right) = 0 \tag{A2}$$

To derive power G, the expression of J_{out} from the energy balance (eq. A1) is inserted into the entropy balance (eq.A2).

$$G = J_{in}\left(\frac{T_s - T_r}{T_s}\right) - \sigma T_s \tag{A3}$$

According to the second law of thermodynamics, $\sigma \geq 0$. The maximum power (G_{carnot}) is achieved when there is no entropy generation inside the engine $\sigma = 0$. So, the expression of G_{carnot} is

$$G_{carnot} = J_{in}\left(\frac{T_s - T_r}{T_s}\right) \tag{A4}$$

The Carnot efficiency, maximum efficiency due to the maximum power, is given by:

$$\eta_{carnot} = \frac{G_{carnot}}{J_{in}} = \left(\frac{T_s - T_r}{T_s}\right) \tag{A5}$$

A.2. Power of a dissipative heat engine

In a dissipative engine, the generated mechanical work dissipates within the engine and increases its internal energy. The dissipative heat in such an engine, even if it dissipates near the hot reservoir, does not act as an additional source with input heat, G. It increases the internal energy of the system. The radiative-convective process of the land-atmosphere behaves as a dissipative engine. Considering the same engine as above but with an

additional process of frictional dissipation (D) and additional term, we get the state of internal energy of the system (ΔU). The power generated for the convection motion in the engine is given by G.

According to the first law of thermodynamics, the energy budget of a heat engine:

$$\Delta U = \Delta J - G \tag{A6}$$

Where, ΔU is the internal energy of the engine, ΔJ is the amount of heat flux, and G is the power develops for mechanical work.

For a dissipative heat engine in a steady state,D is added because the total power for convective motion is dissipated as heat within the engine.

$$\Delta U = J_{in} - J_{out} - G + D \tag{A7}$$

In a steady state, $G = D$ because the total power for convective motion is dissipated as heat within the engine. In addition,$G = D = \Delta U$ because the generated heat from frictional dissipation cannot be used as an additional heat source to generate work but converts into the internal energy of the engine to raise its temperature. So, eq. (A7) becomes:

$$\Delta U = J_{in} - J_{out} = D = G \tag{A8}$$

The associated entropy budget of a dissipative heat engine is given by the entropy associated with the change in the internal energy of the engine at an effective temperature of the heat engine T_a, entropy associated with the input energy from the hot reservoir at the temperature T_s, entropy from the emitted heat at the temperature T_r, entropy due to frictional dissipation term D at T_a, and the irreversible entropy production ΔS_{irr} within the engine other than due to frictional dissipation.

$$\frac{\Delta U}{T_a} = \frac{J_{in}}{T_s} - \frac{J_{out}}{T_r} + \frac{D}{T_a} + \Delta S_{irr} \tag{A9}$$

For a system where the irreversible entropy generates only due to the frictional dissipation, entropy through non-frictional dissipation is zero ($\sigma_{irr} = 0$). In that case, the maximum power or Carnot limit of the dissipative heat engine is estimated by assuming $\sigma_{irr} = 0$ in the (A9), eliminating J_{out} in eq. (A10) with the expression from eq. (A8), and using $G = D$ in steady-state.

$$G = J_{in}\frac{T_a}{T_s}.\frac{T_s - T_r}{T_r} - \Delta U.\frac{T_a - T_r}{T_r} \tag{A10}$$

For the land-atmosphere dry convective system, T_a is the mean temperature of the atmosphere. As the convective engine is operated in the lower atmosphere, it is closer to the surface temperature and can be reasonably assumed as $T_a \approx T_s$. The atmospheric heat storage represents the internal energy of the engine ($\Delta U = \Delta Q_a$). For a dry convective system, the Sensible heat represents the heat source ($J_{in} = H$), and the temperature of the cold reservoir is given by the dry sink temperature T_{dry}. Thus, from (A10), we get the expression of the limit on power generation of the dissipative convective engine in which irreversible entropy generates only because of the irreversible frictional dissipation.

$$G_d = (H - \Delta Q_a).\frac{T_s - T_{dry}}{T_d} \tag{A11}$$

Further, from eq. (A7), $G = D = \Delta Q_a$, eq. (A11) becomes:

$$G_d = H.\frac{T_s - T_{dry}}{T_s} = \Delta Q_a \tag{A12}$$

A.3. The storage heat distribution in the land-atmosphere dry convective system

The energy budget equation of the surface is given by:

$$\Delta Q_s = R_s - R_{l,net} - H - LE \tag{A13}$$

The energy budget of the atmosphere is given by:

$$\Delta Q_a = R_{l,net} + H + LE - R_{l,out} \tag{A14}$$

And the entropy budget is given by:

$$\frac{\Delta Q_a}{T_e} = \frac{H}{T_s} + \frac{LE}{T_{dry}} + \frac{R_{l,net}}{T_{dry}} - \frac{R_{lout}}{T_{dry}} + \frac{D_k}{T_e} + \Delta S_{dif} \tag{A15}$$

T_e is the temperature of the engine. The T_e is approximated by T_s as the process is taking place close to the surface. The total energy balance of the system and heat storage (ΔQ_{total}) in the land-atmospheric system during the dry convection is given by adding eqs. (A13) and (A14):

$$\Delta Q_{total} = \Delta Q_a + \Delta Q_s = R_s - R_{lout} \tag{A16}$$

According to eq. (A12), we assumed that the heat storage in the atmosphere (ΔQ_a) or an increase in the internal energy of a dry convective system only occurs due to the changes within the heat engine. However, a parallel radiative transfer of energy $R_{l,net}$, independent of the heat engine, also contributes to heat storage changes in the atmosphere. It is essential to understand the change in the power limit given by eq. (12) due to $R_{l,net}$. According to the study (Kleidon and Renner, 2018), in both cases where the atmosphere is opaque to $R_{l,net}$ or completely transparent does not change the power limit given by the eq. (A12).

A.4. Linearization of longwave radiative heat transfer ($R_{l,net}$)

$$R_{l,net} = L_{\uparrow} - L_{\downarrow} \tag{A17}$$

$$R_{l,net} = \sigma {T_s}^4 - \frac{3}{4}\tau\sigma {T_{dry}}^4 \tag{A18}$$

The surface is assumed as a blackbody with thermal emission given by $\sigma {T_s}^4$. σ is the Stefan-Boltzmann constant ($\sigma = 5.67 \times 10^{-8}$). $L_{\downarrow} = \frac{3}{4}\tau\sigma {T_{dry}}^4$ gives the longwave radiative flux towards the surface. τ is the longwave optical depth (or thickness) of the atmosphere. In our model, we use $L_{\downarrow}$ as the input. However, many parameterization schemes exist to estimate $L_{\downarrow}$ from on-ground meteorological variables(Loridan et al., 2011; Offerle et al., 2003).

To estimate maximum convective power, the expression of net longwave radiation is linearized using first-order Taylor expansion around the sink temperature(T_{dry})

$$\sigma {T_s}^4 \approx \sigma {T_{dry}}^4 + K_d\left(T_s - T_{dry}\right) \tag{A19}$$

Where K_d is a first order constant given by $K_d = 4\sigma {T_{dry}}^3$.

Combining eqs. (A17), (A18), and (A19), we get the linear approximation of $R_{l,net}$ in terms of temperature difference.

$$R_{l,net} = R_{l,0} + K_d\left(T_s - T_{dry}\right) \tag{A20}$$

With constant $R_{l,0}$ given as:

$$R_{l,0} = \sigma {T_{dry}}^4 - L_{\downarrow} \tag{A21}$$

The atmospheric temperature at which the heat is radiated out from the dry convective engine is the effective dry sink temperature (T_{dry}). It is the temperature with the highest radiative entropy to radiate out from the dry convective heat engine with associated emission of radiation given by radiative flux ($R_{l,out} = \sigma {T_{dry}}^4$).

So eq. (A21) becomes:

$$R_{l,0} = R_{l,out} - L_{\downarrow} \tag{A22}$$

$$K_d = \frac{4R_{l,out}}{T_{dry}} \tag{A23}$$

And,

$$T_{dry} = \left(\frac{R_{l,out}}{\sigma}\right)^{\frac{1}{4}} \tag{A24}$$

A.5. Turbulent fluxes from the maximum convective power limit

The dry convection in the lower atmosphere transports heat as Sensible heat flux and passively transports latent heat flux until water vapour condenses. The surface also cools through the radiative transfer of heat $R_{l,net}$. In a complete land-atmospheric convective system boundary, the heat engine and $R_{l,net}$ reduces the temperature difference of boundaries. The sensible heat flux in dry convection is derived by maximizing the convective power $\left(\frac{dG}{dH} = 0\right)$. The eq. (A13) from eq. (A20) can be written as:

$$\Delta Q_s = R_s - R_{l,0} - K_d\left(T_s - T_{dry}\right) - H - LE \tag{A25}$$

From eq. (A25), we can express the temperature difference as:

$$T_s - T_{dry} = \frac{R_s - R_{l,0} - H - LE - \Delta Q_s}{K_d} \tag{A26}$$

From eq. 7 in theory section, we can replace LE_{opt} in terms of H_{opt} in eq. (A26)

$$T_s - T_{dry} = \frac{R_s - R_{l,0} - H\left(1 + \frac{s}{\gamma}\right) - \Delta Q_s}{K_d} \tag{A27}$$

To obtain the maximum convective power of the engine driven by the sensible heat flux (H), G_d. from the eq. (12) and (A27) can be written as:

$$G_d = H.\frac{R_s - R_{l,0} - H\left(1 + \frac{s}{\gamma}\right) - \Delta Q_s}{T_s K_d} \tag{A28}$$

Appendix A. Supplementary data

Supplementary data to this article can be found online at https://doi.org/10.1016/j.rse.2023.113659.

References

Abdolghafoorian, A., Farhadi, L., Bateni, S.M., Margulis, S., Xu, T., 2017. Characterizing the effect of vegetation dynamics on the bulk heat transfer coefficient to improve variational estimation of surface turbulent fluxes. J. Hydrometeorol. 18, 321–333. https://doi.org/10.1175/JHM-D-16-0097.1.

Ando, T., Ueyama, M., 2017. Surface energy exchange in a dense urban built-up area based on two-year eddy covariance measurements in Sakai, Japan. Urban Clim. 19, 155–169. https://doi.org/10.1016/j.uclim.2017.01.005.

Baldocchi, D., Falge, E., Gu, L., Olson, R., Hollinger, D., Running, S., Anthoni, P., Bernhofer, C., Davis, K., Evans, R., Fuentes, J., Goldstein, A., Katul, G., Law, B., Lee, X., Malhi, Y., Meyers, T., Munger, W., Oechel, W., Paw, U.K.T., Pilegaard, K., Schmid, H.P., Valentini, R., Verma, S., Vesala, T., Wilson, K., Wofsy, S., 2001. FLUXNET: a new tool to study the temporal and spatial variability of ecosystem-scale carbon dioxide, water vapor, and energy flux densities. Bull. Am. Meteorol. Soc. 82, 2415–2434. https://doi.org/10.1175/1520-0477(2001)082<2415:FANTTS>2.3.CO;2.

Bastiaanssen, W.G.M., Menenti, M., Feddes, R.A., Holtslag, A.A.M., 1998. A remote sensing surface energy balance algorithm for land (SEBAL). 1. Formulation. J. Hydrol. 212–213, 198–212. https://doi.org/10.1016/S0022-1694(98)00253-4.

Bastiaanssen, W.G.M., Pelgrum, H., Wang, J., Ma, Y., Moreno, J.F., Roerink, G.J., van der Wal, T., 1998. A remote sensing surface energy balance algorithm for land (SEBAL).2. Validation. J. Hydrol. 212–213, 213–229. https://doi.org/10.1016/S0022-1694(98)00254-6.

Bateni, S.M., Entekhabi, D., 2012. Relative efficiency of land surface energy balance components. Water Resour. Res. 48, 1–8. https://doi.org/10.1029/2011WR011357.

Bateni, S.M., Entekhabi, D., 2012. Surface heat flux estimation with the ensemble Kalman smoother : Joint estimation of state and parameters, 48, 1–16. https://doi.org/10.1029/2011WR011542.

Bateni, S.M., Entekhabi, D., Jeng, D.-S., 2013. Variational assimilation of land surface temperature and the estimation of surface energy balance components. J. Hydrol. 481, 143–156. https://doi.org/10.1016/j.jhydrol.2012.12.039.

Best, M.J., Abramowitz, G., Johnson, H.R., Pitman, A.J., Balsamo, G., Boone, A., Cuntz, M., Decharme, B., Dirmeyer, P.A., Dong, J., Ek, M., Guo, Z., Haverd, V., van Den Hurk, B.J.J., Nearing, G.S., Pak, B., Peters-Lidard, C., Santanello, J.A., Stevens, L., Vuichard, N., 2015. The plumbing of land surface models: benchmarking model performance. J. Hydrometeorol. 16, 1425–1442. https://doi.org/10.1175/JHM-D-14-0158.1.

Bister, M., Renno, N., Pauluis, O., Emanuel, K., 2011. Comment on Makarieva et al. "A critique of some modern applications of the Carnot heat engine concept: The dissipative heat engine cannot exist". Proc. R. Soc. A Math. Phys. Eng. Sci. 467, 1–6. https://doi.org/10.1098/rspa.2010.0087.

Boone, A., Samuelsson, P., Gollvik, S., Napoly, A., Jarlan, L., Brun, E., Decharme, B., 2017. The interactions between soil–biosphere–atmosphere land surface model with a multi-energy balance (ISBA-MEB) option in SURFEXv8 – part 1: model description. Geosci. Model Dev. 10, 843–872. https://doi.org/10.5194/gmd-10-843-2017.

Carlson, T., 2007. An overview of the "Triangle method" for estimating surface evapotranspiration and soil moisture from satellite imagery. Sensors 7, 1612–1629. https://doi.org/10.3390/s7081612.

Carrera, M.L., Bélair, S., Bilodeau, B., 2015. The Canadian Land Data Assimilation System (CaLDAS). J. Hydrometeorol. 16, 1293–1314. https://doi.org/10.1175/JHM-D-14-0089.1.

Chow, W., 2017. Eddy covariance data measured at the CAP LTER flux tower located in the west Phoenix, AZ neighborhood of Maryvale from 2011-12-16 through 2012-12-31 ver 1 [WWW Document]. Environ. Data Initiat. https://doi.org/10.6073/pasta/fed17d67583eda16c439216ca40b0669.

Chu, H., Baldocchi, D.D., John, R., Wolf, S., Reichstein, M., 2017. Fluxes all of the time? A primer on the temporal representativeness of FLUXNET. J. Geophys. Res. Biogeosci. 122, 289–307. https://doi.org/10.1002/2016JG003576.

Conte, L., Renner, M., Brando, P., Oliveira dos Santos, C., Silvério, D., Kolle, O., Trumbore, S.E., Kleidon, A., 2019. Effects of tropical deforestation on surface energy balance partitioning in southeastern Amazonia estimated from maximum convective power. Geophys. Res. Lett. 46, 4396–4403. https://doi.org/10.1029/2018GL081625.

Davin, E.L., Maisonnave, E., Seneviratne, S.I., 2016. Is land surface processes representation a possible weak link in current regional climate Models? Environ. Res. Lett. 11 https://doi.org/10.1088/1748-9326/11/7/074027.

Division, T., Alamos, L., 1999. First- and Second-Order Conservative Remapping Schemes for Grids in Spherical Coordinates 2204–2210.

Duveiller, G., Hooker, J., Cescatti, A., 2018. A dataset mapping the potential biophysical effects of vegetation cover change. Sci. Data 5, 1–15. https://doi.org/10.1038/sdata.2018.14.

Engstrom, R., Hope, A., Kwon, H., Harazono, Y., Mano, M., Oechel, W., 2006. Modeling evapotranspiration in Arctic coastal plain ecosystems using a modified BIOME-BGC model. J. Geophys. Res. Biogeosciences 111, 1–20. https://doi.org/10.1029/2005JG000102.

Forzieri, G., Alkama, R., Miralles, D.G., Cescatti, A., 2018. Satellites reveal contrasting responses of regional climate to the widespread greening of Earth. Science80-.) 360, 1180–1184. https://doi.org/10.1126/science.aap9664.

Franssen, H.J.H., Stöckli, R., Lehner, I., Rotenberg, E., Seneviratne, S.I., 2010. Energy balance closure of eddy-covariance data: a multisite analysis for European FLUXNET stations. Agric. For. Meteorol. 150, 1553–1567. https://doi.org/10.1016/j.agrformet.2010.08.005.

Friedl, M., Sulla-Menashe, D., 2015. MCD12C1 MODIS/Terra+Aqua Land Cover Type Yearly L3 Global 0.05Deg CMG V006 [Data set] [WWW Document]. NASA EOSDIS L. Process. DAAC. https://doi.org/10.5067/MODIS/MCD12C1.006.

Gillies, R.R., Kustas, W.P., Humes, K.S., 1997. A verification of the "triangle" method for obtaining surface soil water content and energy fluxes from remote measurements of the normalized difference vegetation index (NDVI) and surface e. Int. J. Remote Sens. 18, 3145–3166. https://doi.org/10.1080/014311697217026.

Grimmond, C.S.B., Blackett, M., Best, M.J., Barlow, J., Baik, J.-J., Belcher, S.E., Bohnenstengel, S.I., Calmet, I., Chen, F., Dandou, A., Fortuniak, K., Gouvea, M.L., Hamdi, R., Hendry, M., Kawai, T., Kawamoto, Y., Kondo, H., Krayenhoff, E.S., Lee, S.-H., Loridan, T., Martilli, A., Masson, V., Miao, S., Oleson, K., Pigeon, G., Porson, A., Ryu, Y.-H., Salamanca, F., Shashua-Bar, L., Steeneveld, G.-J., Tombrou, M., Voogt, J., Young, D., Zhang, N., 2010. The international urban energy balance models comparison project: first results from phase 1. J. Appl. Meteorol. Climatol. 49, 1268–1292. https://doi.org/10.1175/2010JAMC2354.1.

Gupta, M., Chauhan, T., Murtugudde, R., Ghosh, S., 2020. Pollutants control the process networks of urban environmental-meteorology. Environ. Res. Lett. 16 https://doi.org/10.1088/1748-9326/abce28.

Gutowski, W.J., Ullrich, P.A., Hall, A., Leung, L.R., O'Brien, T.A., Patricola, C.M., Arritt, R.W., Bukovsky, M.S., Calvin, K.V., Feng, Z., Jones, A.D., Kooperman, G.J., Monier, E., Pritchard, M.S., Pryor, S.C., Qian, Y., Rhoades, A.M., Roberts, A.F., Sakaguchi, K., Urban, N., Zarzycki, C., 2020. The ongoing need for high-resolution regional climate models: process understanding and stakeholder information. Bull. Am. Meteorol. Soc. 101, E664–E683. https://doi.org/10.1175/BAMS-D-19-0113.1.

Heidkamp, M., Chlond, A., Ament, F., 2018. Closing the energy balance using a canopy heat capacity and storage concept- a physically based approach for the land component JSBACHv3.11. Geosci. Model Dev. 11, 3465–3479. https://doi.org/10.5194/gmd-11-3465-2018.

Hersbach, H., Bell, B., Berrisford, P., Hirahara, S., Horányi, A., Muñoz-Sabater, J., Nicolas, J., Peubey, C., Radu, R., Schepers, D., Simmons, A., Soci, C., Abdalla, S., Abellan, X., Balsamo, G., Bechtold, P., Biavati, G., Bidlot, J., Bonavita, M., Chiara, G., Dahlgren, P., Dee, D., Diamantakis, M., Dragani, R., Flemming, J., Forbes, R., Fuentes, M., Geer, A., Haimberger, L., Healy, S., Hogan, R.J., Hólm, E., Janisková, M., Keeley, S., Laloyaux, P., Lopez, P., Lupu, C., Radnoti, G., Rosnay, P., Rozum, I., Vamborg, F., Villaume, S., Thépaut, J., 2020. The ERA5 global reanalysis. Q. J. R. Meteorol. Soc. 146, 1999–2049. https://doi.org/10.1002/qj.3803.

Higgins, C.W., 2012. A-posteriori analysis of surface energy budget closure to determine missed energy pathways. Geophys. Res. Lett. 39, 1–5. https://doi.org/10.1029/2012GL052918.

Huang, J., Mendoza, B., Daniel, J.S., Nielsen, C.J., Rotstayn, L., Wild, O., 2013. In: Anthropogenic and natural radiative forcing. Clim. Chang. 2013 Phys. Sci. Basis Work. Gr. I Contrib. to Fifth Assess. Rep. Intergov. Panel Clim. Chang. 9781107057, pp. 659–740. https://doi.org/10.1017/CBO9781107415324.018.

Jiang, L., Islam, S., 2001. Estimation of surface evaporation map over southern Great Plains using remote sensing data. Water Resour. Res. 37, 329–340. https://doi.org/10.1029/2000WR900255.

Jiménez, C., Prigent, C., Mueller, B., Seneviratne, S.I., McCabe, M.F., Wood, E.F., Rossow, W.B., Balsamo, G., Betts, A.K., Dirmeyer, P.A., Fisher, J.B., Jung, M., Kanamitsu, M., Reichle, R.H., Reichstein, M., Rodell, M., Sheffield, J., Tu, K., Wang, K., 2011. Global intercomparison of 12 land surface heat flux estimates. J. Geophys. Res. Atmos. 116, 1–27. https://doi.org/10.1029/2010JD014545.

Jung, M., Koirala, S., Weber, U., Ichii, K., Gans, F., Camps-Valls, G., Papale, D., Schwalm, C., Tramontana, G., Reichstein, M., 2019. The FLUXCOM ensemble of global land-atmosphere energy fluxes. Sci. Data 6, 1–14. https://doi.org/10.1038/s41597-019-0076-8.

Jung, M., Reichstein, M., Margolis, H.A., Cescatti, A., Richardson, A.D., Arain, M.A., Arneth, A., Bernhofer, C., Bonal, D., Chen, J., Gianelle, D., Gobron, N., Kiely, G., Kutsch, W., Lasslop, G., Law, B.E., Lindroth, A., Merbold, L., Montagnani, L., Moors, E.J., Papale, D., Sottocornola, M., Vaccari, F., Williams, C., 2011. Global patterns of land-atmosphere fluxes of carbon dioxide, latent heat, and sensible heat derived from eddy covariance, satellite, and meteorological observations. J. Geophys. Res. Biogeosciences 116, 1–16. https://doi.org/10.1029/2010JG001566.

Kalma, J.D., McVicar, T.R., McCabe, M.F., 2008. Estimating land surface evaporation: a review of methods using remotely sensed surface temperature data. Surv. Geophys. 29, 421–469. https://doi.org/10.1007/s10712-008-9037-z.

Kato, S., Loeb, N.G., Rose, F.G., Doelling, D.R., Rutan, D.A., Caldwell, T.E., Yu, L., Weller, R.A., 2013. Surface irradiances consistent with CERES-derived top-of-atmosphere shortwave and longwave irradiances. J. Clim. 26, 2719–2740. https://doi.org/10.1175/JCLI-D-12-00436.1.

Kleidon, A., 2016. Thermodynamic Foundations of the Earth System, Thermodynamic Foundations of the Earth System. Cambridge University Press, Cambridge. https://doi.org/10.1017/CBO9781139342742.

Kleidon, A., Renner, M., 2018. Diurnal land surface energy balance partitioning estimated from the thermodynamic limit of a cold heat engine. Earth Syst. Dyn. 9, 1127–1140. https://doi.org/10.5194/esd-9-1127-2018.

Kleidon, A., Renner, M., 2013a. Thermodynamic limits of hydrologic cycling within the earth system: concepts, estimates and implications. Hydrol. Earth Syst. Sci. 17, 2873–2892. https://doi.org/10.5194/hess-17-2873-2013.

Kleidon, A., Renner, M., 2013b. A simple explanation for the sensitivity of the hydrologic cycle to surface temperature and solar radiation and its implications for global climate change. Earth Syst. Dyn. 4, 455–465. https://doi.org/10.5194/esd-4-455-2013.

Kleidon, A., Renner, M., Porada, P., 2014. Estimates of the climatological land surface energy and water balance derived from maximum convective power. Hydrol. Earth Syst. Sci. 18, 2201–2218. https://doi.org/10.5194/hess-18-2201-2014.

L'Ecuyer, T.S., Beaudoing, H.K., Rodell, M., Olson, W., Lin, B., Kato, S., Clayson, C.A., Wood, E., Sheffield, J., Adler, R., Huffman, G., Bosilovich, M., Gu, G., Robertson, F., Houser, P.R., Chambers, D., Famiglietti, J.S., Fetzer, E., Liu, W.T., Gao, X., Schlosser, C.A., Clark, E., Lettenmaier, D.P., Hilburn, K., 2015. The observed state of the energy budget in the early twenty-first century. J. Clim. 28, 8319–8346. https://doi.org/10.1175/JCLI-D-14-00556.1.

Liang, S., Liang, S., Zhang, X., Wang, K., Zhang, X., Wild, M., 2010. Review on estimation of land surface radiation and energy budgets from ground measurement, remote sensing and model simulations. IEEE JSel. Top. Appl. Earth Obs. Remote Sens. 3, 225–240. https://doi.org/10.1109/JSTARS.2010.2048556.

Lindroth, A., Mölder, M., Lagergren, F., 2010. Heat storage in forest biomass improves energy balance closure. Biogeosciences 7, 301–313. https://doi.org/10.5194/bg-7-301-2010.

Loeb, N.G., Johnson, G.C., Thorsen, T.J., Lyman, J.M., Rose, F.G., Kato, S., 2021. Satellite and ocean data reveal marked increase in Earth's heating rate. Geophys. Res. Lett. 48, 1–8. https://doi.org/10.1029/2021GL093047.

Loridan, T., Grimmond, C.S.B., Offerle, B.D., Young, D.T., Smith, T.E.L., Järvi, L., Lindberg, F., 2011. Local-scale urban meteorological parameterization scheme (LUMPS): longwave radiation parameterization and seasonality-related developments. J. Appl. Meteorol. Climatol. 50, 185–202. https://doi.org/10.1175/2010JAMC2474.1.

Roberts, S.M., Oke, T.R., Grimmond, C.S.B., Voogt, J.A., 2006. Comparison of four methods to estimate urban heat storage. J. Appl. Meteorol. Climatol. 45, 1766–1781. https://doi.org/10.1175/JAM2432.1.

Ma, Y., Liu, S., Song, L., Xu, Z., Liu, Y., Xu, T., Zhu, Z., 2018. Estimation of daily evapotranspiration and irrigation water efficiency at a landsat-like scale for an arid irrigation area using multi-source remote sensing data. Remote Sens. Environ. 216, 715–734. https://doi.org/10.1016/j.rse.2018.07.019.

Mallick, K., Jarvis, A., Fisher, J.B., Tu, K.P., Boegh, E., Niyogi, D., 2013. Latent heat flux and canopy conductance based on penman-monteith, priestley-Taylor equation, and Bouchet's complementary hypothesis. J. Hydrometeorol. 14, 419–442. https://doi.org/10.1175/JHM-D-12-0117.1.

Mallick, K., Jarvis, A.J., Boegh, E., Fisher, J.B., Drewry, D.T., Tu, K.P., Hook, S.J., Hulley, G., Ardö, J., Beringer, J., Arain, A., Niyogi, D., 2014. A surface temperature initiated closure (STIC) for surface energy balance fluxes. Remote Sens. Environ. 141, 243–261. https://doi.org/10.1016/j.rse.2013.10.022.

Martens, B., Miralles, D.G., Lievens, H., Van Der Schalie, R., De Jeu, R.A.M., Fernández-Prieto, D., Beck, H.E., Dorigo, W.A., Verhoest, N.E.C., 2017. GLEAM v3: satellite-based land evaporation and root-zone soil moisture. Geosci. Model Dev. 10, 1903–1925. https://doi.org/10.5194/gmd-10-1903-2017.

Mauder, M., Foken, T., Cuxart, J., 2020. Surface-Energy-Balance Closure over Land: A Review, Boundary-Layer Meteorology. Springer, Netherlands. https://doi.org/10.1007/s10546-020-00529-6.

Meier, R., Davin, E.L., Lejeune, Q., Hauser, M., Li, Y., Martens, B., Schultz, N.M., Sterling, S., Thiery, W., 2018. Evaluating and improving the Community Land Model's sensitivity to land cover. Biogeosciences 15, 4731–4757. https://doi.org/10.5194/bg-15-4731-2018.

Meier, R., Davin, E.L., Swenson, S.C., Lawrence, D.M., Schwaab, J., 2019. Biomass heat storage dampens diurnal temperature variations in forests. Environ. Res. Lett. 14, 84026. https://doi.org/10.1088/1748-9326/ab2b4e.

Meyers, T.P., Hollinger, S.E., 2004. An assessment of storage terms in the surface energy balance of maize and soybean. Agric. For. Meteorol. 125, 105–115. https://doi.org/10.1016/j.agrformet.2004.03.001.

Miralles, D.G., Holmes, T.R.H., De Jeu, R.A.M., Gash, J.H., Meesters, A.G.C.A., Dolman, A.J., 2011. Global land-surface evaporation estimated from satellite-based observations. Hydrol. Earth Syst. Sci. 15, 453–469. https://doi.org/10.5194/hess-15-453-2011.

Miralles, D.G., Jiménez, C., Jung, M., Michel, D., Ershadi, A., McCabe, M.F., Hirschi, M., Martens, B., Dolman, A.J., Fisher, J.B., Mu, Q., Seneviratne, S.I., Wood, E.F., Fernández-Prieto, D., 2016. The WACMOS-ET project – part 2: evaluation of global terrestrial evaporation data sets. Hydrol. Earth Syst. Sci. 20, 823–842. https://doi.org/10.5194/hess-20-823-2016.

Moore, C.J., Fisch, G., 1986. Estimating heat storage in Amazonian tropical forest. Agric. For. Meteorol. 38, 147–168. https://doi.org/10.1016/0168-1923(86)90055-9.

Mu, Q., Heinsch, F.A., Zhao, M., Running, S.W., 2007. Development of a global evapotranspiration algorithm based on MODIS and global meteorology data. Remote Sens. Environ. 111, 519–536. https://doi.org/10.1016/j.rse.2007.04.015.

Mueller, B., Hirschi, M., Jimenez, C., Ciais, P., Dirmeyer, P.A., Dolman, A.J., Fisher, J.B., Jung, M., Ludwig, F., Maignan, F., Miralles, D.G., McCabe, M.F., Reichstein, M., Sheffield, J., Wang, K., Wood, E.F., Zhang, Y., Seneviratne, S.I., 2013. Benchmark products for land evapotranspiration: LandFlux-EVAL multi-data set synthesis. Hydrol. Earth Syst. Sci. 17, 3707–3720. https://doi.org/10.5194/hess-17-3707-2013.

Mueller, B., Seneviratne, S.I., 2014. Systematic land climate and evapotranspiration biases in CMIP5 simulations. Geophys. Res. Lett. 41, 128–134. https://doi.org/10.1002/2013GL058055.

Niu, G.-Y., Yang, Z.-L., Mitchell, K.E., Chen, F., Ek, M.B., Barlage, M., Kumar, A., Manning, K., Niyogi, D., Rosero, E., Tewari, M., Xia, Y., 2011. The community Noah land surface model with multiparameterization options (Noah-MP): 1. Model description and evaluation with local-scale measurements. J. Geophys. Res. 116, D12109. https://doi.org/10.1029/2010JD015139.

Offerle, B., Grimmond, C.S.B., Oke, T.R., 2003. Parameterization of net all-wave radiation for urban areas. J. Appl. Meteorol. 42, 1157–1173. https://doi.org/10.1175/1520-0450(2003)042<1157:PONARF>2.0.CO;2.

Oke, T.R., Cleugh, H.A., 1987. Urban heat storage derived as energy balance residuals. Bound.-Layer Meteorol. 233–245. https://doi.org/10.1007/BF00116120.

Oke, T.R., Kalanda, B.D., Steyn, D.G., 1981. Parameterization of heat storage in urban areas. Urban Ecol. 5, 45–54. https://doi.org/10.1016/0304-4009(81)90020-6.

Pastorello, G., Trotta, C., Canfora, E., Chu, H., Christianson, D., Cheah, Y.W., Poindexter, C., Chen, J., Elbashandy, A., Humphrey, M., Isaac, P., Polidori, D., Ribeca, A., van Ingen, C., Zhang, L., Amiro, B., Ammann, C., Arain, M.A., Ardö, J., Arkebauer, T., Arndt, S.K., Arriga, N., Aubinet, M., Aurela, M., Baldocchi, D., Barr, A., Beamesderfer, E., Marchesini, L.B., Bergeron, O., Beringer, J., Bernhofer, C., Berveiller, D., Billesbach, D., Black, T.A., Blanken, P.D., Bohrer, G., Boike, J., Bolstad, P.V., Bonal, D., Bonnefond, J.M., Bowling, D.R., Bracho, R., Brodeur, J., Brümmer, C., Buchmann, N., Burban, B., Burns, S.P., Buysse, P., Cale, P., Cavagna, M., Cellier, P., Chen, S., Chini, I., Christensen, T.R., Cleverly, J., Collalti, A., Consalvo, C., Cook, B.D., Cook, D., Coursolle, C., Cremonese, E., Curtis, P.S., D'Andrea, E., da Rocha, H., Dai, X., Davis, K.J., De Cinti, B., de Grandcourt, A., De Ligne, A., De Oliveira, R.C., Delpierre, N., Desai, A.R., Di Bella, C. M., di Tommasi, P., Dolman, H., Domingo, F., Dong, G., Dore, S., Duce, P., Dufrêne, E., Dunn, A., Dušek, J., Eamus, D., Eichelmann, U., ElKhidir, H.A.M., Eugster, W., Ewenz, C.M., Ewers, B., Famulari, D., Fares, S., Feigenwinter, I., Feitz, A., Fensholt, R., Filippa, G., Fischer, M., Frank, J., Galvagno, M., Gharun, M., Gianelle, D., Gielen, B., Gioli, B., Gitelson, A., Goded, I., Goeckede, M., Goldstein, A. H., Gough, C.M., Goulden, M.L., Graf, A., Griebel, A., Gruening, C., Grünwald, T., Hammerle, A., Han, S., Han, X., Hansen, B.U., Hanson, C., Hatakka, J., He, Y., Hehn, M., Heinesch, B., Hinko-Najera, N., Hörtnagl, L., Hutley, L., Ibrom, A., Ikawa, H., Jackowicz-Korczynski, M., Janouš, D., Jans, W., Jassal, R., Jiang, S., Kato, T., Khomik, M., Klatt, J., Knohl, A., Knox, S., Kobayashi, H., Koerber, G., Kolle, O., Kosugi, Y., Kotani, A., Kowalski, A., Kruijt, B., Kurbatova, J., Kutsch, W.L., Kwon, H., Launiainen, S., Laurila, T., Law, B., Leuning, R., Li, Yingnian, Liddell, M., Limousin, J.M., Lion, M., Liska, A.J., Lohila, A., López-Ballesteros, A., López-Blanco, E., Loubet, B., Loustau, D., Lucas-Moffat, A., Lüers, J., Ma, S., Macfarlane, C., Magliulo, V., Maier, R., Mammarella, I., Manca, G., Marcolla, B., Margolis, H.A., Marras, S., Massman, W., Mastepanov, M., Matamala, R., Matthes, J.H., Mazzenga, F., McCaughey, H., McHugh, I., McMillan, A.M.S., Merbold, L., Meyer, W., Meyers, T., Miller, S.D., Minerbi, S., Moderow, U., Monson, R.K., Montagnani, L., Moore, C.E., Moors, E., Moreaux, V., Moureaux, C., Munger, J.W., Nakai, T., Neirynck, J., Nesic, Z., Nicolini, G., Noormets, A., Northwood, M., Nosetto, M., Nouvellon, Y., Novick, K., Oechel, W., Olesen, J.E., Ourcival, J.M., Papuga, S.A., Parmentier, F.J., Paul-Limoges, E., Pavelka, M., Peichl, M., Pendall, E., Phillips, R.P., Pilegaard, K., Pirk, N., Posse, G., Powell, T., Prasse, H., Prober, S.M., Rambal, S., Rannik, Ü., Raz-Yaseef, N., Reed, D., de Dios, V.R., Restrepo-Coupe, N., Reverter, B.R., Roland, M., Sabbatini, S., Sachs, T., Saleska, S.R., Sánchez-Cañete, E. P., Sanchez-Mejia, Z.M., Schmid, H.P., Schmidt, M., Schneider, K., Schrader, F., Schroder, I., Scott, R.L., Sedlák, P., Serrano-Ortíz, P., Shao, C., Shi, P., Shironya, I., Siebicke, L., Šigut, L., Silberstein, R., Sirca, C., Spano, D., Steinbrecher, R., Stevens, R.M., Sturtevant, C., Suyker, A., Tagesson, T., Takanashi, S., Tang, Y., Tapper, N., Thom, J., Tiedemann, F., Tomassucci, M., Tuovinen, J.P., Urbanski, S., Valentini, R., van der Molen, M., van Gorsel, E., van Huissteden, K., Varlagin, A., Verfaillie, J., Vesala, T., Vincke, C., Vitale, D., Vygodskaya, N., Walker, J.P., Walter-Shea, E., Wang, H., Weber, R., Westermann, S., Wille, C., Wofsy, S., Wohlfahrt, G., Wolf, S., Woodgate, W., Li, Yuelin, Zampedri, R., Zhang, J., Zhou, G., Zona, D., Agarwal, D., Biraud, S., Torn, M., Papale, D., 2020. The FLUXNET2015 dataset and the ONEFlux processing pipeline for eddy covariance data. Sci. data 7, 225. https://doi.org/10.1038/s41597-020-0534-3.

Paul, S., Ghosh, S., Mathew, M., Devanand, A., Karmakar, S., Niyogi, D., 2018. Increased spatial variability and intensification of extreme monsoon rainfall due to urbanization. Sci. Rep. 8, 1–10. https://doi.org/10.1038/s41598-018-22322-9.

Pauluis, O., Held, I.M., 2002. Entropy budget of an atmosphere in radiative–convective equilibrium. Part I: Maximum work and frictional dissipation. J. Atmos. Sci. 59 (2), 125–139.

Pauluis, O., Held, I.M., 2002. Entropy budget of an atmosphere in radiative–convective equilibrium. Part II: Latent heat transport and moist processes. J. Atmos. Sci. 59 (2), 140–149.

Priestley, C.H.B., Taylor, R.J., 1972. On the assessment of surface heat flux and evaporation using large-scale parameters. Mon. Weather Rev. 100, 81–92. https://doi.org/10.1175/1520-0493(1972)100<0081:otaosh>2.3.co;2.

Purdy, A.J., Fisher, J.B., Goulden, M.L., Famiglietti, J.S., 2016. Ground heat flux: an analytical review of 6 models evaluated at 88 sites and globally. J. Geophys. Res. Biogeosci. 121, 3045–3059. https://doi.org/10.1002/2016JG003591.

Rahman, M.M., Zhang, W., 2019. Review on estimation methods of the Earth's surface energy balance components from ground and satellite measurements. J. Earth Syst. Sci. 128, 1–22. https://doi.org/10.1007/s12040-019-1098-5.

Rennó, N.O., Ingersoll, A.P., 1996. Natural convection as a heat engine: a theory for CAPE. J. Atmos. Sci. 53, 572–585. https://doi.org/10.1175/1520-0469(1996)053<0572:NCAAHE>2.0.CO;2.

Rodell, M., Houser, P.R., Jambor, U., Gottschalck, J., Mitchell, K., Meng, C.-J., Arsenault, K., Cosgrove, B., Radakovich, J., Bosilovich, M., Entin, J.K., Walker, J.P., Lohmann, D., Toll, D., 2004. The global land data assimilation system. Bull. Am. Meteorol. Soc. 85, 381–394. https://doi.org/10.1175/BAMS-85-3-381.

Running, S.W., Mu, Q., Zhao, M., 2017. MOD16A2 MODIS/Terra Net Evapotranspiration 8-Day L4 Global 500m SIN Grid V006[Data set] [WWW Document]. NASA EOSDIS L. Process. DAAC. https://doi.org/10.5067/MODIS/MOD16A2.006.

Rutan, D.A., Kato, S., Doelling, D.R., Rose, F.G., Nguyen, L.T., Caldwell, T.E., Loeb, N.G., 2015. CERES synoptic product: methodology and validation of surface radiant flux. J. Atmos. Ocean. Technol. 32, 1121–1143. https://doi.org/10.1175/JTECH-D-14-00165.1.

Sandholt, I., Rasmussen, K., Andersen, J., 2002. A simple interpretation of the surface temperature/vegetation index space for assessment of surface moisture status. Remote Sens. Environ. 79, 213–224. https://doi.org/10.1016/S0034-4257(01)00274-7.

Schuckmann, K.Von, Cheng, L., Palmer, M.D., Hansen, J., Tassone, C., 2020. Heat stored in the Earth system : where does the energy go ? 2013–2041.

Schultz, N.M., Lawrence, P.J., Lee, X., 2017. Global satellite data highlights the diurnal asymmetry of the surface temperature response to deforestation. J. Geophys. Res. Biogeosci. 122, 903–917. https://doi.org/10.1002/2016JG003653.

Sheffield, J., Wood, E.F., Roderick, M.L., 2012. Little change in global drought over the past 60 years. Nature 491, 435–438. https://doi.org/10.1038/nature11575.

Siemann, A.L., Chaney, N., Wood, E.F., 2018. Development and validation of a long-term, global, terrestrial sensible heat flux dataset. J. Clim. 31, 6073–6095. https://doi.org/10.1175/JCLI-D-17-0732.1.

Song, L., Kustas, W.P., Liu, S., Colaizzi, P.D., Nieto, H., Xu, Z., Ma, Y., Li, M., Xu, T., Agam, N., Tolk, J.A., Evett, S.R., 2016. Applications of a thermal-based two-source energy balance model using priestley-Taylor approach for surface temperature partitioning under advective conditions. J. Hydrol. 540, 574–587. https://doi.org/10.1016/j.jhydrol.2016.06.034.

Stephens, G.L., Li, J., Wild, M., Clayson, C.A., Loeb, N., Kato, S., L'Ecuyer, T., Stackhouse, P.W., Lebsock, M., Andrews, T., 2012. An update on Earth's energy balance in light of the latest global observations. Nat. Geosci. 5, 691–696. https://doi.org/10.1038/ngeo1580.

Stoy, P.C., Mauder, M., Foken, T., Marcolla, B., Boegh, E., Ibrom, A., Arain, M.A., Arneth, A., Aurela, M., Bernhofer, C., Cescatti, A., Dellwik, E., Duce, P., Gianelle, D., van Gorsel, E., Kiely, G., Knohl, A., Margolis, H., Mccaughey, H., Merbold, L., Montagnani, L., Papale, D., Reichstein, M., Saunders, M., Serrano-Ortiz, P., Sottocornola, M., Spano, D., Vaccari, F., Varlagin, A., 2013. A data-driven analysis of energy balance closure across FLUXNET research sites: the role of landscape scale heterogeneity. Agric. For. Meteorol. 171–172, 137–152. https://doi.org/10.1016/j.agrformet.2012.11.004.

Su, Z., 2002. The surface energy balance system (SEBS) for estimation of turbulent heat fluxes. Hydrol. Earth Syst. Sci. 6, 85–100. https://doi.org/10.5194/hess-6-85-2002.

Sun, L., Liang, S., Yuan, W., Chen, Z., 2013. Improving a penman-monteith evapotranspiration model by incorporating soil moisture control on soil evaporation in semiarid areas. Int. J. Digit. Earth 6, 134–156. https://doi.org/10.1080/17538947.2013.783635.

Tang, R., Li, Z., Tang, B., 2010. An application of the Ts–VI triangle method with enhanced edges determination for evapotranspiration estimation from MODIS data in arid and semi-arid regions: implementation and validation. Remote Sens. Environ. 114, 540–551. https://doi.org/10.1016/j.rse.2009.10.012.

Trenberth, K.E., Fasullo, J.T., Kiehl, J., 2009. Earth's global energy budget. Bull. Am. Meteorol. Soc. 90, 311–323. https://doi.org/10.1175/2008BAMS2634.1.

Von Schuckmann, K., Palmer, M.D., Trenberth, K.E., Cazenave, A., Chambers, D., Champollion, N., Hansen, J., Josey, S.A., Loeb, N., Mathieu, P.P., Meyssignac, B., Wild, M., 2016. An imperative to monitor Earth's energy imbalance. Nat. Clim. Chang. 6, 138–144. https://doi.org/10.1038/nclimate2876.

Wang, K., Li, Z., Cribb, M., 2006. Estimation of evaporative fraction from a combination of day and night land surface temperatures and NDVI: a new method to determine the Priestley-Taylor parameter. Remote Sens. Environ. 102, 293–305. https://doi.org/10.1016/j.rse.2006.02.007.

Wild, M., 2020. The global energy balance as represented in CMIP6 climate models. Clim. Dyn. 55, 553–577. https://doi.org/10.1007/s00382-020-05282-7.

Wild, M., Folini, D., Hakuba, M.Z., Schär, C., Seneviratne, S.I., Kato, S., Rutan, D., Ammann, C., Wood, E.F., König-Langlo, G., 2015. The energy balance over land and oceans: an assessment based on direct observations and CMIP5 climate models. Clim. Dyn. 44, 3393–3429. https://doi.org/10.1007/s00382-014-2430-z.

Wild, M., Folini, D., Schär, C., Loeb, N., Dutton, E.G., König-Langlo, G., 2013. The global energy balance from a surface perspective. Clim. Dyn. 40, 3107–3134. https://doi.org/10.1007/s00382-012-1569-8.

Xu, T., Bateni, S.M., Neale, C.M.U., Auligne, T., Liu, S., 2018. Estimation of turbulent heat fluxes by assimilation of land surface temperature observations from GOES satellites into an ensemble Kalman smoother framework. J. Geophys. Res. Atmos. 123, 2409–2423. https://doi.org/10.1002/2017JD027732.

Xu, T., He, X., Bateni, S.M., Auligne, T., Liu, S., Xu, Z., Zhou, J., Mao, K., 2019. Mapping regional turbulent heat fluxes via variational assimilation of land surface temperature data from polar orbiting satellites. Remote Sens. Environ. 221, 444–461. https://doi.org/10.1016/j.rse.2018.11.023.

Xu, T., Liu, S., Liang, S., Qin, J., 2011. Improving predictions of water and heat fluxes by assimilating MODIS land surface temperature products into the common land model. J. Hydrometeorol. 12, 227–244. https://doi.org/10.1175/2010JHM1300.1.

Yi, L., Qiulin, L., Kun, Y., Wenqing, X., Xiaolu, Z., Chunxue, S., Yuanting, X., 2019. Science of the total environment thermodynamic analysis of air-ground and water-ground energy exchange process in urban space at micro scale. Sci. Total Environ. 694, 133612 https://doi.org/10.1016/j.scitotenv.2019.133612.

Zimba, H., Coenders-Gerrits, M., Banda, K., Hulsman, P., van de Giesen, N., Nyambe, I., Savenije, H., 2022. On the importance of phenology in the miombo ecosystem: evaluation of open-source satellite evaporation models. Hydrol. Earth Syst. Sci. Discuss. 2022, 1–42.